DYNAMICS AND DIFFUSION IN HARD AND STOCHASTIC STRUCTURED SOLVENTS

by

Benjamin Dean Mahala

A dissertation submitted to Johns Hopkins University
in conformity with the requirements for the degree of
Doctor of Philosophy

Baltimore, Maryland
October, 2019

Abstract

Using molecular dynamics (MD), we study the dynamics of solvent systems that are complex, but tractable. We look at the translational and rotational diffusion of a spherocylindrical tracer in through a sea of fixed scatterers in two and three dimensions. We show that previously used order parameters do not capture the observed diffusion in three dimensions and provide a correction factor to the order parameter to capture the observed motion. We then observe how the addition of an implicit Langevin solvent changes the relative diffusion. We observe where the Langevin solvent is a good coarse-grained approximation to the hard sphere solvent and a diffusion anomaly generated by the mixture of the two solvents. We also study how a reactive particle (RP) in a double well potential interacts with a solvent undergoing stochastic hard collisions (SHC). We observe how changing the effective solvent softness parameter changes the rate of the reaction, and how this compares to the Kramers' theoretical rate for the system.

Advisor: Dr. Rigoberto Hernandez

Readers: Dr. David R. Yarkony, Dr. Paul J. Dagdigian

Acknowledgments

Finishing this thesis would not be possible without the support of Rigoberto Hernandez, my advisor. I thank you for financially supporting me as I completed this work and for thinking of me and your other group members when you moved to Johns Hopkins. I would have never made it here if not for you. I also thank Dr. Alex Popov for our excellent conversations and his impressively in depth knowledge of every physical system I encounter. I thank Galen Craven and Ashley Tucker for writing the code that eventually ended up in these projects and Matt Hagy for teaching me what he knew about coding when I first arrived in the group.

Table of Contents

Abstract ii

Acknowledgments iv

Table of Contents v

List of Figures ix

1 Introduction 1

1.1 Motivation 1

1.2 Thesis Structure and Objectives 4

2 The Lorentz Gas 7

2.1 Background 7

2.2 Extensions and Anomalies 12

2.3 Conclusion 16

3 Order parameters in the diffusion of rods through two and three dimensional fixed scatterers 18

3.1 Introduction 18

3.2 Theory 22

  3.2.1 The LG Model 22

  3.2.2 Transport Coefficients 23

  3.2.3 Order Parameters 25

3.3 Numerical Methods 27

  3.3.1 Numerical Integration and Propagation 27

  3.3.2 Algorithms for Determining Transport Coefficients . . 28

  3.3.3 Numerics in Determination of Diffusion Coefficients . 31

3.4 Results 34

  3.4.1 Tracer in Two Dimensions 34

  3.4.2 Tracer in Three Dimensions 37

3.5 Discussion 40

4 Molecular dynamics of a mixed solvent system: diffusion anomalies and coarse graining **47**

4.1 Introduction 47

4.2 Theory 49

  4.2.1 Order Parameters 49

4.3 Numerical Methods 50

  4.3.1 Numerical Integration and Propagation 50

  4.3.2 Algorithms for Determining Transport Coefficients . . 53

    4.3.2.1 Translational Diffusion 53

4.3.2.2 Rotational Diffusion 57

4.4 Results and Discussion 58

4.5 Conclusions 61

5 Insight into transport anomalies in the stochastic Lorentz gas with guidance from periodic orbits 65

5.1 Introduction 65

5.2 Theory 67

5.2.1 Categorizing Orbits 67

5.2.2 Formula and Applications 68

5.3 Discussion and Conclusion 72

6 Solvent softness effects on unimolecular chemical reaction rate constants 76

6.1 Introduction 76

6.2 Theory 79

6.2.1 The Stochastic Hard Collision (SHC) Solvent 79

6.2.2 Kramers' Turnover Theory 80

6.3 Numerical Methods 82

6.3.1 Reactive Particle and Solvent Bath 82

6.3.2 Reaction and Rate Constant Calculation 84

6.3.3 Numerical Analysis 86

6.4 Results and Discussion 90

6.5 Conclusions 95

7 Conclusion and Future Work **100**

7.1 Concluding Remarks 100

7.2 Future Work 101

Appendix **104**

Vita **114**

List of Figures

2.1 A short trajectory of the Sinai billiard model, a dynamical system similar to the Lorentz gas where a point particle moves in a confined box with a spherical scatterer stuck in the center. Nearly every trajectory is provably ergodic.[3] 8

2.2 The reduced translational and rotational diffusion coefficients of an infinitely thin rod vs reduced density of point scatterers in 2D that clearly shows the translational diffusion increasing and rotational diffusion decreases with increasing reduced density — the enhanced diffusion regime.[12] 15

2.3 The reduced translational (blue triangles) and rotational (red squares) diffusion of a thick rod in spheres as function of reduced density in 2D. Notice the enhanced diffusion regime shown in fig 2.2 survives the presence of excluded volume.[13] 16

3.1 A typical MSD (blue and red dots) for a 2D simulation as a function of displacement time Δt. Specifically, the parameters are: $n^* = 0.1$, $L = 14.142$ Å, $\sigma_s = 0.5$ Å, $\sigma_t = 0.5$ Å. The blue points are those excluded from the fitting due to not being in the linear regime. The black line is the linear fit of the red points with a slope of 1769.02 ± 0.24 ps. 29

3.2 A typical velocity autocorrelation function (red dots) for a 2D simulation as a function of displacement time Δt at the same parameters as figure 3.1. The black line is the exponential fit with a decay time of 25.615 ± 0.009 ps. 30

3.3 The 2D and 3D diffusion constants obtained on a periodic box with increasing size and corresponding increasing number of scatterers. The tracer length is held fixed at $L = 31.623$ Å and 21.544 Å in 2D and 3D, respectively. The number of scatterers in the largest finite box is N_0 equal to 1960 and 3375 in 2D and 3D, respectively. In all cases, the box size and N satisfy the condition that the scatterer density is 0.001, and $n^* = 1.0$. . . 34

3.4 The 2D reduced diffusion constant as a function of tracer length at three different constant values of n^* scaled by a characteristic length L_0 = 28.3, 63.2 and 200 Å in each panel from top to bottom, respectively. Notice that the reduced diffusion is a good order parameter at large tracer length (low density at constant n^*) because the curves are flat in this region, and hence D_{com} is a constant with respect to L. 35

3.5 The dependence of the 2D translational diffusion constant of the tracer on the effective length L_{eff} at constant n^*_{eff}. In this case $n^*_{\text{eff}} = 1.0$, $\sigma_s = \sigma_t = 0.5$ Å. The blue line is the linear fit, and the black line is a constant fit. The constant fit is within the error bars of the power law fit, $\frac{D_{\text{com}}}{vL_{\text{eff}}} \sim .003\ L_{\text{eff}}$, which is within 1.5 σ from zero. 37

3.6 The 3D reduced diffusion constant as a function of tracer length at constant values of n^* — as also displayed for the 2D case in figure 3.4 — scaled by a characteristic length L_0 = 7.0, 29.2, 63.0 Å from top to bottom, respectively. The dashed line is a linear fit to the data, with R^2 values > 0.999 for all plots. Note that the reduced diffusion is nowhere a good order parameter in 3D. 38

3.7 The 3D translational diffusion constant of the tracer as a function of the effective tracer length L_{eff} at constant n^*_{eff}. The parameters are $n^*_{\text{eff}} = 1.0$, $\sigma_s = \sigma_t = 0.5$ Å. The black line is the linear fit, $\frac{D_{\text{com}}}{vL_{\text{eff}}} \sim .24\ L_{\text{eff}}$, with a slope that is about 100 times that in the 2D case. 39

3.8 The 3D reduced diffusion constant is displayed as a contour and the 3D-surface plots over the two-dimensional domain of γn^* and scatterer and tracer radius σ^{-1}. The black lines on the surface indicate constant L as indicated, and also correspond to the values of γn^* on the bottom left axis. The vertices of the lines on the upper surface are explicitly computed to which the surface has been fitted. The dashed contour lines represent lines of constant reduced diffusion and potential order parameters. 40

4.1 Typical MSD Fit on a log-log plot, allowing the fit of the diffusion exponent as well as the diffusion coefficient to be extracted. The red points indicate the long time regime, whereas the blue points indicate the short to medium regime. The dashed line is the fit. Taken from a 2D system of hard spheres with $n^*_{\text{ex}} = 1.0$ 55

4.2 Typical VAC (red) and corresponding exponential fit (dashed line). The diffusion is extracted from quadrature integration of the red points, while the effective friction is extracted from the exponential fit using equation 4.15. Notice the negative anti-correlation VAC regime that is characteristic of a dense hard sphere system. This regime cannot be approximated by a Langevin solvent and is the reason the Langevin solvent is increasingly inaccurate at representing hard dynamics at high density. Taken from a 2D system of hard spheres with $n^*_{\text{ex}} = 1.0$ 56

4.3 This plot shows the interaction of the dual Langevin-Lorentz solvent compared to the pure Langevin solvent as a function of translational friction. The red line is the friction which corresponds to the pure 2D Lorentz gas solvent with $n^* = 1.0$. The black line is to show that there is a correspondence between the Lorentz solvent and a Lanvegin solvent using the same effective friction. The blue line is the theoretical result from the Einstein equation for a Langevin system with that friction. The circles are MSD power law fits, the squares correspond to MSD linear fits, and the triangles correspond to VAC fits. This plot shows that at $n^* = 1.0$, the translational dynamics of the Langevin solvent are a good approximation to the Lorentz gas. 58

4.4 This figure shows the reduced diffusion coefficient of a 2D Lorentz gas, a pure Langevin solvent whose friction is set to the effective friction of the corresponding Lorentz gas, and a dual Langevin-Lorentz solvent with the same effective friction. The triangles refer to D extracted from the VAC, the circles have D extracted from the log-log MSD, and the squares extracted from the linear MSD fit. At low n^*_{ex}, which corresponds to low friction on the order of 0.1 ps^{-1}, the Langevin solvent and the hard sphere solvent have good agreement, with the dual solvent having less then half of the diffusion as each solvent in isolation. At higher n^*_{ex}, excluded volume effects start taking over and reducing the diffusion far below the corresponding effective Langevin friction. Notice the hints of the diffusion anomaly at higher densities, as the dual solvent overtakes the pure hard sphere solvent. This is explored in figure 4.5 59

4.5 This is a plot exemplifying the diffusion anomaly in the 2D Langevin-Lorentz gas. The Lorentz solvent system has an $n^*_{\text{ex}} = 4.0$ for every point, while the Langevin friction is varied from 0 to 0.6. A Langevin friction of 0 implies a pure hard sphere, which has a diffusion coefficient of $D^0_{\text{com}} = 0.96 \frac{2}{ps}$. As the Langevin friction is increases, the diffusion coefficient anomalously increases instead of decreasing. The red spheres are the MSD log-log fit, the blue squares are the linear MSD fit, and the green triangles are the VAC quadrature integration . 60

4.6 This is a plot showing the rotational diffusion coefficient under the same conditions as figure 4.5. The anomalous diffusion observed in that figure does not appear to extend to rotation, as the rotational diffusion is monotonically decreasing with additional friction. 61

5.1 This figure demonstrates the difference between standing and traveling orbits on an infinite periodic lattice. The red line is the standing orbit $\overline{13}$. The blue line is the traveling orbit $\overline{1234}$. Orbits like the blue line contribute to the overall diffusion coefficient while red orbits detract from the diffusion. 68

5.2 This figure shows how ϕ is defined with respect to a incident collision with a scatterer of radius σ_{S}. The relevant stability factor $r(\phi) = \frac{2}{\sigma_{\mathrm{S}}\cos(\phi)}$. $\phi = 0$ implies to complete reversal of the tracer's velocity. The singularity at $\phi = \frac{\pi}{2}$ is due to the fact that glancing collisions are not well defined in the hard-sphere potential. 70

6.1 A typical velocity autocorrelation function (solid red curve) for the reactive particle in a harmonic potential solvated by 300 SHC particles compared to the least-squares fit (dashed black curve) of the cosine exponential form in Eq. 6.11. This particular system correspond to $T = 300\,\mathrm{K}$, $\delta = 0.25$, and $\epsilon = 2kT$, for which $\omega = 6.951$ ps^{-1},$\phi = 0.1316$, $\gamma = 0.9892$ ps^{-1} with an $R^2 = 0.999159$. 87

6.2 A characteristic PMF obtained by Monte Carlo (MC) sampling for a reactive particle in the SHC solvent under the same conditions as Fig. 6.1. The wells were fit to a quartic potential (using only the red points ovelapping the dashed line) resulting in values of $a = 6.157$, $b = -23.132$, $c = -78.255$, $d = 187.79$ $e = 764.87$, $W = 905.06$ with residual equal to $R^2 = 0.999813$ Similarly, the barrier was fit to a quartic potential (using only the blue points ovelapping the dashed line) resulting in values of $a = 14.692$, $b = -71.611$, $c = 15.979$, $d = 175.277$ $e = 717.816$, $W = 904.774$ with residual equal to $R^2 = 0.975657$ 89

6.3 The friction extracted from the VAC (red points) and FAC (blue points) fits. The potential the RP experiences is a harmonic with the same spring constant as the RP would feel at the bottom of the well in the double well potential with $\epsilon = 2\ k_{\mathrm{B}}T$. All of these simulations are done with 1 RP and 300 solvent particles. 90

6.4 A triple plot showing how the relevant factors change between the bare potential given in eqn. 6.7 and the MC simulations. The top plot references the effective spring constant at the bottom of the well, k_1, the middle plot references the spring constant at the top of the barrier, k_2, and the bottom plot references the distance between the top of the barrier and the bottom of the well, ϵ. Each color represents a different ϵ, with red representing $\epsilon = 2k_{\mathrm{B}}T$ and so on. 92

6.5 The unimolecular rate constant for barrier crossing, K, as a function of δ for $\epsilon = 3k_{\mathrm{B}}T$. All simulations have 1 RP and 300 solvent particles. 93

6.6 The unimolecular rate constant for barrier crossing, K, as a function of δ. The red and blue points are MD numerical results. The yellow and magenta points are the theoretical results using Kramers' rate theory. They differ by the method used to compute the friction. The points that use the friction as extracted from the VAC are magenta and the yellow use the FAC to extract the friction. The labels on the right denote the value of ϵ in units of $k_{\mathrm{B}}T$. All simulations have 1 RP and 300 solvent particles. 93

6.7 Theoretical factors constirbuting to Kramers' rate, κ_{PGH} and Y, vs. δ. κ_{PGH} and Y are numbers between 0 and 1. In the under damped regime of low γ, Y dominates the rate and κ_{PGH} is close to 1. In the over damped regime of high γ the reverse happens. These results are from $\epsilon = 3k_{\mathrm{B}}T$, but is representative of all ϵ values studied here. 95

A.1 γ_{eff} vs. number density ρ for a 2D scatterer at various n^*. $\sigma_{\mathrm{T}} = \sigma_{\mathrm{S}} = 0.5$ Angstroms. 105

A.2 D_{R} vs. number density ρ for a 2D scatterer at various n^*. $\sigma_{\mathrm{T}} = \sigma_{\mathrm{S}} = 0.5$ Angstroms. D_{R} is extracted from the RAC via $F_{\mathrm{RAC}}(\Delta t) = \cos(\omega \Delta t) e^{-2D_{\mathrm{R}}\Delta t}$. 106

A.3 D_{R} vs. number density ρ for a 2D scatterer with various L_{eff} at constant $n^*_{\mathrm{ex}} = 1$. $\sigma_{\mathrm{T}} = \sigma_{\mathrm{S}} = 0.5$ D_{R} is extracted from the RAC via $F_{\mathrm{RAC}}(\Delta t) = \cos(\omega \Delta t) e^{-2D_{\mathrm{R}}\Delta t}$ called the cos and exponential fit and $F_{\mathrm{RAC}}(\Delta t) = e^{-2D_{\mathrm{R}}\Delta t}$, which is called the pure exponential fit. D_{R} is not invariant at constant n^* at low lengths, most likely due to the tracer beginning to approximate a sphere, as spheres have fundimentally different rotational properties compared to spherocylinders. 106

A.4 L_{eff} vs. average collision time $\langle t_{\mathrm{coll}} \rangle$ at constant $n^*_{\mathrm{ex}} = 1$. $\sigma_{\mathrm{T}} = \sigma_{\mathrm{S}} = 0.5$ Angstroms. Note that at constant n^*_{ex}, L_{eff} is inversly proportional to the number density of scatterers, so increasing $\langle t_{\mathrm{coll}} \rangle$ with increasing L_{eff} is not unexpected. 107

A.5 $\frac{D_{\mathrm{com}}}{vL}$ vs. t_{step}. Although the MSD data is noisy, it is clear that changing the time step size does not effect D. 107

A.6 $\frac{D_{\mathrm{R}}L}{v}$ vs. t_{step}. The reduced rotational diffusion coefficient is clearly not a function of the time step. 108

A.7 $\frac{D_{\mathrm{R}}L}{v}$ vs. $\frac{L}{L_0}$ in 3D where $L_0 = 7.0, 29.2, 63.0$ Å from top to bottom, respectively. 108

A.8 $\frac{D_{\mathrm{com}}}{vL}$ vs. N at constant density $\rho = 0.001$ in 3D. The flatness implies the box is large enough to ignore finite size effects. . . 109

A.9 $\frac{D_{\mathrm{R}}L}{v}$ vs. N at constant density $\rho = 0.001$ in 3D. The flatness implies the box is large enough to ignore finite size effects. . . 109

A.10 $\frac{D_{\mathrm{com}}}{vL}$ vs. t_{step}. The flatness implies the stepsize does not cause any issues with the transport. 110

A.11 $\frac{D_{\mathrm{R}}L}{v}$ vs. t_{step}. The flatness implies the stepsize does not cause any issues with the transport. 110

A.12 $\log D_{\mathrm{R}}$ vs. $\log \gamma_{\omega}$. For a 2D rod in a pure Langevin solvent with no spheres. At high friction the Debye approximation holds and D_{R} decreases linearly with friction. At low friction, the system assumes a static equilibrium distribution regardless of friction. 111

A.13 The Rotational Autocorrelation function with 2nd order Legendre polynomial for a 3D thick tracer in hard spheres with $\gamma n^* = 0.1$. Note the large and long tail that any Langevin system is incapable of generating at any friction. This implies that low density rotational motion in the hard sphere solvent is fundamentally different from rotational motion in a Langevin solvent. It is not possible to map this motion to an effective Langevin friction. 111

A.14 Characteristic reactive particle velocity distribution post equilibration. $\delta = 0$ 300 scatterers, equilibrated for $10,000$ collisions. The red histogram is the post equilibration velocity of the RP over $100,000$ equilibration trajectories split into 100 bins. The black line is the fit to a Maxwell-Boltzmann velocity distribution with effective temperature of $298K$. Error from $300K$ due to inexact fit and finite bin size. Used for generating post equilibration velocities below. 112

A.15 The average post equilibration temperature for the tracer or scatterers in the SHC system equilibrated in a harmonic well vs. the number of collisions the system is equilibrated for. When the temperature reaches 300 K the system is properly equilibrating. Number of scatterers is 300, $\delta = 0$. 112

A.16 The average post equilibration temperature of tracers or scatterers in the SHC system equilibrated in a harmonic well vs. the number of scatterers in the system. The movement towards system temperature of 300 implies the vanishing of finite size effects. Equilibrated for $10,000$ collisions. 113

Chapter 1

Introduction

1.1 Motivation

Understanding dynamical systems is fundamental to understanding the world around us. However, for large systems like us, the fundamental laws of nature are too complex to solve analytically or simulate directly. In order to understand the world we live in, we must find ways of modeling systems that respect the implicit scales we are interested in. This requires understanding the world of classical mechanics, as well as the fundamental non-classical laws of our universe.

Although the rules are more intuitive then quantum mechanics, classical mechanics is no simple master. Long before electronic computers gave us the first graphical glimpse of simulated chaos, the apparent simplicity of Kepler's elliptical orbits lead to numerous attempts to find analytic solutions for systems of more then two interacting bodies. Some progress was made, including a general solution in the form of an infinite series which, unfortunately, converges far too slowly to be of practical use.[1,2] However, the holy grail: a simple, useful, analytic solution for a nonlinear system of many interacting bodies, was never found.

Around the same time, statistical mechanics appeared to offer a solution: if the dynamics of many body systems were too complicated, perhaps the statistics of these systems would be better behaved? In many cases, a full mathematical edifice of statistical thermodynamic understanding can be created. However, some of the first electronic computer simulations of nonlinear dynamical systems gave a shocking result: they looked almost periodic, and did not equipartition.[3] These systems were supposed to quickly equilibrate, but instead showed rich long-time non-equilibrium behavior. At the heart of this paradox lies the fact that a nonlinear, chaotic system is not a *random* system, and can have arbitrarily long-lived correlations. Having a valid average when integrating to infinity does not mean that the system will approach that average in a reasonable time. Simple dynamical laws are no guarantee that the average of an observable exists in the infinite limit — adding a set of numbers and dividing by the set size does not necessarily generate a physically meaningful average!

Ultimately, there are no cheap tricks to understanding non-equilibrium dynamical systems: they must be understood on their own terms. The tools of understanding are not static and have progressed significantly over the years, from using periodic orbit theory to understand the nature of diffusion or the structure of the Helium atom to using molecular dynamic simulations to understand large solvated electrically striped particles.[4–7]

In any case, the choice of model system is of utmost importance. Choosing a model be as close as possible to the system of interest is safe, but often such models have too many degrees of freedom to practically integrate. Choosing a model that is less directly connected to your system of interest but that shares many dynamical properties is called coarse graining (CG). There are many coarse graining methodologies with various degrees of rigor.[8] As with understanding dynamics, there is no universal scheme for removing unnecessary degrees of freedom that is always accurate. A first step to extracting useful dynamics from a CG system is meeting the requirement of dynamical consistency. A CG procedure is dynamically consistent if the full dynamics replicate between the CG and fine grained system; matching static or structural properties is not good enough to insure consistent dynamics. In practice this means paying close attention to non-equilibrium dynamical factors and not just equilibrium structure properties.

In this work, we look at the dynamical properties of coarse grained structured solvents through the lens of order parameters and transport coefficients. In particular, we look at extensions to the Lorentz gas, the stochastic hard collision solvent, and mixtures of the Lorentz gas and well-studied Langevin solvent.[9,10] The goal is to gain knowledge of these systems on their own terms and to see how simple dynamical laws can generate complex but understandable behavior. Our choice of model systems might, at first glance, seem surprisingly simple. That apparent simplicity is an illusion hiding rich non-equilibrium dynamics that have been studied for over 100 years yet still manage to surprise.

1.2 Thesis Structure and Objectives

Understanding complex dynamics requires both theoretical analysis and numerical simulation. We begin in Chapter 2 by discussing the history and previous work done on the Lorentz gas solvent, starting with its inception in 1905 and moving through modern theory and simulation techniques.[11] We then present our published work on order parameters in the two and three dimensional Lorentz gas system in chapter 3.[9] Chapter 4 discusses our further extensions and exploration of the Lorentz gas system with an additional Langevin solvent in two dimensions; observing how this dual solvent system impacts the dynamics of the tracer. Chapter 5 rounds out our discussion of the Lorentz gas with a theoretical exploration of applied periodic orbit theory aiming to isolate the fundamental causes of some of the unusual behavior observed in the previous chapters. Chapter 6 begins the discussion of another system of interest: the stochastic hard collision (SHC) solvent. We explore this unique solvent's effect on a unimolecular reaction rates by immersing the reactive particle in the SHC solvent and observing how varying the softness effects the rate. We then compare these rates with the theoretical rates derived from Kramers' turnover theory.[12] In Chapter 7 we conclude with an overview of the main results and an exploration of future work.

References

(1) Barrow-Green, J. *Historia Mathematica* **2010**, *37*, 164–203.

(2) Gowers, T.; Barrow-Green, J.; Leader, I., *The Princeton Companion to Mathematics*; Princeton University Press: 2008, pp 726–728.

(3) Ford, J. *Physics Reports* **1992**, *213*, 271–310.

(4) Hagy, M. C.; Hernandez, R. *J. Chem. Phys* **2014**, *140*, 034701.

(5) Yamamoto, T.; Kaneko, K. *Phys. Rev. Lett.* **1993**, *70*, 1928–1931.

(6) Cvitanović, P.; Gaspard, P.; Schreiber, T. *Chaos* **1992**, *2*, 85–90.

(7) Cvitanović, P.; Artuso, R.; Mainieri, R.; Tanner, G.; Vattay, G., *Chaos: Classical and Quantum*; Niels Bohr Institute: Copenhagen, 2016.

(8) Brini, E.; Algaer, E. A.; Ganguly, P.; Li, C.; RodrÃ■guez-Roperoa, F.; van der Vegt, N. F. A. *Soft Matt.* **2013**, *9*, 2108–2119.

(9) Mahala, B. D.; Hernadnez, R. *Phys. Rev. E* **2018**, *98*, 042607.

(10) Craven, G. T.; Popov, A. V.; Hernandez, R. *J. Chem. Phys.* **2013**, *138*, 244901.

(11) Lorentz, H. A. *Proc. R. Amst. Acad.* **1905**, *7*, 438–453.

(12) Kramers, H. A. *Physica (Utrecht)* **1940**, *7*, 284–304.

Chapter 2

The Lorentz Gas

2.1 Background

The first appearance of the Lorentz gas was by its namesake, H. A. Lorentz, to model the motion of free electrons in a metal.[1] The idea was simple: since electrons are so light and move so much more quickly than the ions in a metal, the system can be modeled as a single point moving through a sea of frozen spherical scatterers, ignoring electron-electron effects and the motion of the background. In the field of electron transport this model is only somewhat accurate, as quantum and electron-electron interactions turn out to be significant in many cases. However, with the rise of computing and chaos theory in the latter half of the 20th century, studies began to show that even a single tracer moving ballistically through a hard static background can generate dynamics that span the full space of Hamiltonian systems. An example is Sinai billiards: a single point moving ballistically with elastic reflective collisions trapped in a

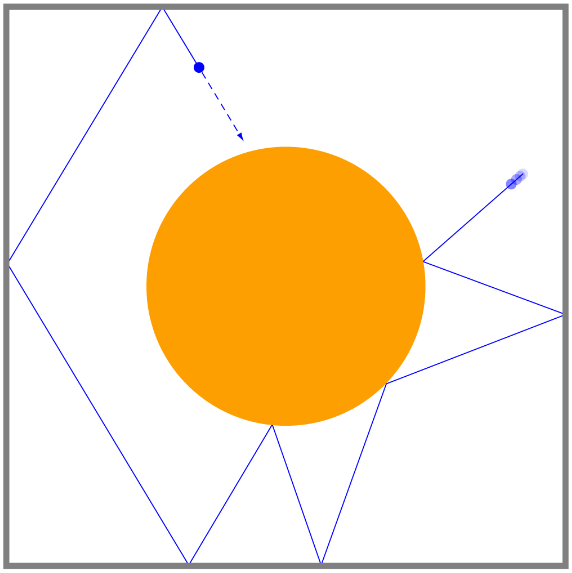

Figure 2.1: A short trajectory of the Sinai billiard model, a dynamical system similar to the Lorentz gas where a point particle moves in a confined box with a spherical scatterer stuck in the center. Nearly every trajectory is provably ergodic.[3]

stadium with convex walls.[2] The fact that complex dynamics can be generated from simple models has made the Lorentz gas and its extensions a sort of fruit fly of the dynamical systems world. It is simple enough to quickly simulate but capable of generating unpredictable dynamics.

A dynamical observable often studied in the context of the Lorentz gas is the diffusion coefficient. Macroscopically, the diffusion coefficient relates the flux of a substance through a boundary to the change in concentration across that boundary. This is known as Fick's law.

$$J = -D\frac{d\rho}{dx} \tag{2.1}$$

where J is a flux (an amount of substance per area per unit time), ρ is the concentration, and D is a constant coefficient with units of area per unit time. This equation makes sense for a series of connected beakers of various concentrations, but seems nonsensical for a single particle moving ballistically. To break diffusion down to the microscopic level, we can look at the mean square displacement (MSD) of the particle after some time. See equation 2.2

$$\mathbf{C}_{\text{MSD}}(\Delta t) = \langle (x(t + \Delta t) - x(t))^2 \rangle_t \tag{2.2}$$

where $x(t)$ is the position of the particle at some arbitrary time t, Δt is a time difference starting at t to some ending time t_{f} and $\langle ... \rangle_t$ implies an average over all possible starting times.

Effectively, the MSD (or rather, its square root) is the answer to the question "if the particle starts at position x and time t and you wait for time Δt, how far on average will the particle be from the starting point?" For a particle moving at constant velocity with no forces or interactions

$$\mathbf{C}_{\text{MSD}}(\Delta t) = v^2 \Delta t^2$$

where v is the particle's root mean squared speed. Einstein showed that if a particle was hit by a large number of small random collisions between the start and end time due to the effects of a solvent, its MSD would instead become,

$$\lim_{\Delta t \to \infty} \mathbf{C}_{\mathrm{MSD}}(\Delta t) = 2dD\Delta t \tag{2.3}$$

where d is the dimensionality of the system and the diffusion constant D can be related to the microscopic parameters of the particle and solvent.[4]

This kind of diffusion is called Brownian motion, and Smoluchowski showed that this motion existed even if the average force from the random collisions was zero due to the random force not favoring a particular direction. This is due to the fact that the average excess force in any one direction follows a binomial distribution and increases with the square root of the number of collisions.[5]

The same reasoning applies to a single tracer moving through a sea of immobile scatterers. So long as collisions are randomly distributed, the long time limit of the MSD is linear in time. The diffusion coefficient can be extracted from equation 2.3 by taking the time derivative at long times.

The MSD is not the only way to extract the diffusion coefficient. In their pioneering work, Green and Kubo were able to show that transport coefficients are fundamentally related to integrals of autocorrelation functions.[6–8] Specifically, the diffusion coefficient can be directly related to the velocity autocorrelation function (VAC)

$$D = \frac{1}{d}\int_0^\infty \langle \vec{v}(t+\Delta t)\cdot\vec{v}(t)\rangle_t \mathbf{d}\Delta t \tag{2.4}$$

where d is the dimensionality and $\vec{v}(t)$ the velocity vector at time t.

In practice, the limits required to calculate the diffusion coefficient from the MSD and VAC are opposite. The MSD requires long trajectories to get a linear fit of the long time region. The VAC requires collecting data very often to get high resolution autocorrelation decay since, although the integral is formally infinite, practical VACs tend to decay to zero within an order of magnitude of the average collision time. Calculating the diffusion coefficient using both methods is valuable, as they will only converge together if a simulation is both running long enough and at high enough resolution, implying the system has fully converged.

Finally, to describe the transport properties of Lorentz gas systems, reduced parameters for the scatterer density and diffusion coefficients are used. Reduced parameters merge multiple system properties into one variable of which the transport properties are a function. For instance, the number density, scatterer radius, and dimensionality can be merged into the reduced density, n^*

$$n^* = \rho\sigma^d \tag{2.5}$$

for a point moving through spherical scatterers of radius σ where ρ is the number density of the scatterers and d is the dimensionality. In addition, the diffusion coefficient itself is often reduced to a unit-less quantity for more direct comparisons between systems. For the system mentioned above, the reduced diffusion coefficient is

$$D_{\text{red}} = \frac{D}{v\sigma} \tag{2.6}$$

where v is the average root mean squared speed of the tracer. These reduced quantities depend on the structure of the system, and must be updated as the systems change.

2.2 Extensions and Anomalies

The original Lorentz gas was a point particle, the tracer, moving through a sea of spherical scatterers. This system is extended to more complicated geometries to explore observables that are not present in the original model. For instance, instead of a point particle, a thin rod can be used to explore how rotation affects the diffusibility of the system.

Moving from a point to a rod breaks the rotational invariance of a spherical tracer and allows the unique determination of a unit vector along the length of the rod, $\hat{\mu}$. If one takes the initial angle of this vector at time t to be $\theta(t)$ and records the change in angle over time, one can generate a mean square angular displacement (MSAD) that is analogous to the MSD for translational motion.

$$\phi^2(\Delta t) \equiv \langle \theta(t + \Delta t) - \theta(t) \rangle_t \tag{2.7}$$

Where θ is the non-periodic angle of the tracer, such that two full rotations starting at $\theta = 0$ yields $\theta = 4\pi$ and not $\theta = 0$, but a full rotation forward and a full rotation back returns θ to zero. The long time MSAD for a rotating tracer undergoing random or pseudo-random collisions is

$$\lim_{\Delta t \to \infty} \phi^2(\Delta t) = 2dD_{\mathrm{R}}\Delta t \tag{2.8}$$

where D_{R} is the rotational diffusion coefficient.

The autocorrelation function of this unit vector generates a similar Green-Kubo relation to the velocity autocorrelation function discussed in equation 2.4. However, extracting the rotational diffusion coefficient is not as simple as it is in the case for translational motion, as a freely rotating object has a non-trivial self correlation function. We define the rotational autocorrelation function (RAC) as follows:

$$\mathbf{C}_1(\Delta t) \equiv \langle \hat{\mu}(t) \cdot \hat{\mu}(t + \Delta t) \rangle_t (\Delta t) \tag{2.9}$$

Ignoring inertia motion, called the Debye approximation, allows a simple expression for the rotational diffusion coefficient as a function of the RAC.[9]

$$\mathbf{C}_1(\Delta t) = e^{2D_{\mathrm{R}}\Delta t} \tag{2.10}$$

The equation for relating $\mathbf{C}_1(\Delta t)$ to D_{R} while accounting for inertial motion is much more complicated, and out of scope for this chapter. See chapter 4 for a more through review of the RAC.

The effect of opening up rotational modes of the tracer does more then generate rotational diffusion; it affects the translational motion of the tracer as well. An extension of the Lorentz gas where an infinitely thin rod moves through a sea of infinitely thin rod scatterers undergoes hard collisions only when it runs into another scatterer side on. This sea of infinitely thin needles has trivial thermodynamic properties, as the system has no long range potential or excluded volume and as such is an ideal gas. The transport properties of this system, however, are very counter-intuitive. Doi and Edwards showed that the translational diffusion coefficient for a rod diverges as the number of

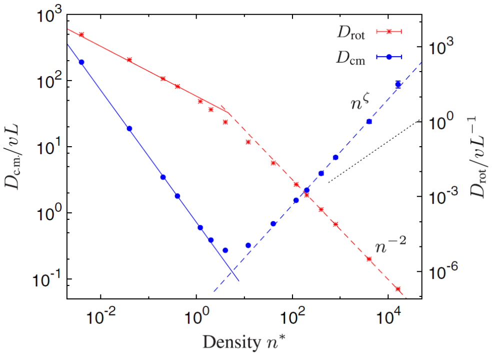

Figure 2.2: The reduced translational and rotational diffusion coefficients of an infinitely thin rod vs reduced density of point scatterers in 2D that clearly shows the translational diffusion increasing and rotational diffusion decreases with increasing reduced density — the enhanced diffusion regime.[12]

rods increases.[10,11]

This result was extended to a single tracer rod in a sea of immobile point scatterers by Höfling and Franosch, who observed the same divergence.[12] Extending the system to include excluded volume effects by making the tracer and scatterers thick smooths the transition to the enhanced diffusion regime and causes the system to become glassy at high densities, but does not eliminate it. See Fig. 2.3 Notice that the onset of the enhanced diffusion regime coincides with a strong suppression of the rotational diffusion coefficient, implying that the rotation, or lack thereof, causes enhanced translational diffusion. Moving from a thick needle in spheres in 2D to a thick needle in spheres in 3D, however, does eliminate the enhanced diffusion regime. This implies that the existence of an enhanced diffusion regime depends strongly on the underlying geometry of the interaction space, and is not merely an

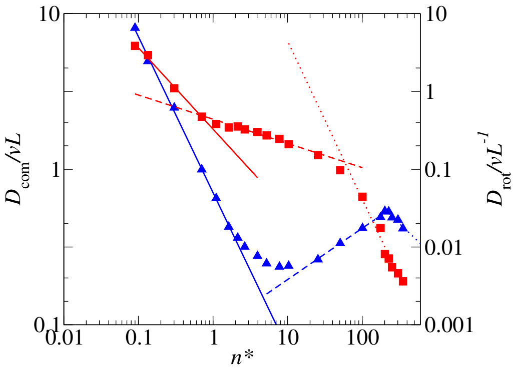

Figure 2.3: The reduced translational (blue triangles) and rotational (red squares) diffusion of a thick rod in spheres as function of reduced density in 2D. Notice the enhanced diffusion regime shown in fig 2.2 survives the presence of excluded volume.[13]

effect of a lack of excluded volume.

2.3 Conclusion

The Lorentz gas has been used as a base for the exploration of many dynamical systems in the world of dynamical simulations. The key of the LG systems are the hard interactions between the tracer and scatterers, which allows the use of efficient collision algorithms while maintaining the emergence of complex dynamical patterns, including counter-intuitive diffusion anomalies. In further chapters, we will explore additional diffusion anomalies and find new ways to extend the LG to softer effective potentials without losing the efficiency of the hard potential.

References

(1) Lorentz, H. A. *Proc. R. Amst. Acad.* **1905**, *7*, 438–453.

(2) Sinai, Y. G. *Russ. Math. Surv* **1970**, *25*, 137–189.

(3) XaoxBits Sinai Billiard. `https://commons.wikimedia.org/wiki/File:SinaiBilliard.png` (accessed 10/03/2019).

(4) Einstein, A. *Annalen der Physik* **1905**, *322*, 549–560.

(5) Smoluchowski, M. M. *Bulletin International de l'AcadÃl'mie des Sciences de Cracovie* **1906**, 577.

(6) Green, M. S. *J. Chem. Phys.* **1954**, *22*, 398.

(7) Kubo, R. *J. Phys. Soc. Jpn.* **1957**, *12*, 570–586.

(8) Zwanzig, R. *Annu. Rev. Phys. Chem.* **1965**, *16*, 67–102.

(9) Hansen, J. P.; McDonald, I. R., *Theory of Simple Liquids*; Academic Press: San Diego, 1986.

(10) Doi, M.; Edwards, S. F. *J. Chem. Soc., Faraday Trans.* **1978**, *74*, 560–570.

(11) Doi, M.; Edwards, S. F. *J. Chem. Soc., Faraday Trans.* **1978**, *74*, 918–932.

(12) Höfling, F.; Frey, E.; Franosch, T. *Phys. Rev. Lett.* **2008**, *101*, 120605.

(13) Tucker, A. K.; Hernandez, R. *J. Phys. Chem.* **2010**, *114*, 9628–9634.

Chapter 3

Order parameters in the diffusion of rods through two and three dimensional fixed scatterers

3.1 Introduction

Characterization of the diffusion of spherocylindrical particles through a solvent is layered in complexity. The asymmetry of the particle structure can lead to asymmetry in its diffusion if the solvent is not uniformly distributed at some characteristic length scale shorter than that of the particle. The nontrivial rotations of the particle about its secondary axes contributes to the dynamics in ways that could lead to asymmetric transport. The nature of the complex solvent can also significantly affect the dynamics of the particle. For example, it could be structured or dissipative in ways that alter its relative rotation, libration, motion along the primary axis direction, and motion across the secondary axes directions. Unraveling this problem does not simply address an interesting theoretical model because, for example, small cylindrical particles are common nanomaterials that have unique electronic properties that are affected by their relative structure and assembly. They often exhibit interesting surface plasmon resonances that can be used for a variety of applications, including lasers and catalysts.[1,2]

We, and others, have used the Lorentz gas (LG) model to describe the solvent as a set of fixed scatterers.[3–8] The LG model was originally introduced by Lorentz in 1905 to model the transport of electrons in a metal and from which he derived a linear Boltzmann equation.[9] The model was used to elaborate the diffusion of light fast particles —the wind— across heavy immovable particles —the trees— so to rigorously construct correlation functions for the corresponding kinetic gas systems.[10] Since then, the LG model has served as a useful benchmark system for kinetic and dynamical theories.[11] The model is simple enough that it is often analytically tractable, if not exactly solvable, and simulations of it are computationally inexpensive. In the context of this work, the LG model describes the environment for the motion of a prolate cylindrical particle through a sea of heavy immobile scatterers organized in either a periodic or aperiodic fashion. The dynamics of the tracer particle in the LG system exhibits surprisingly complex transport behavior. It was discovered early on that the transport coefficients for the LG model system are non-analytic functions of the density, and that any density expansion would diverge in the Dth term where D is the system dimensionality.[12]

For equilibrium structural properties, this model system scales according to a single order parameter, $n^* = \rho\sigma^D$, where σ is the radius of the scatterers and ρ is the density.[12–15] Extensions addressing rods with more complex geometries and self-propulsion have also been explored and is of current interest because of recent advances in the characterization of active matter.[7,16–20] The spherical-tracer order parameter is typically extended for a rod in spheres to 2 and 3 dimensions as $n^* = \rho L^D$ where L is the length of the tracer rod.[21] In this article, we aim to characterize the dynamics of such structured particles within the LG model and test the hypothesis that this or a new modified order parameter provides the appropriate scaled dynamics.

In earlier work by Tucker and Hernandez,[7] the possibility of excluded volume effects on the dynamics of the diffusing particle was introduced into the model by extending the representation of the particle or scatterers from points to spheres, preserving the spherical symmetry of the point particle, but giving it a width. The possibility of effects due to non-spherical structure in the scatter can be introduced by allowing the particle to be a rod with zero radius.

One might expect translational diffusion to be a monotonically decreasing function of the density. However, when the motion of a rod-like particle was investigated by Franosch and coworkers[6,22] an enhanced diffusion regime was discovered in a rod moving through an LG model with point particle scatterers. In this enhanced diffusion regime, increasing the scatterer density leads to increased translational diffusion.[6] An enhanced diffusion regime was also seen for a dense solution of infinitely thin rods due to confinement,[23] though absent in the case of thick scatterers.[8]

Moreno and Kob[3,4] addressed a thick rod LG model with thick (and non-overlapping) spheres that led to glassy dynamics with increasing density. Tucker and Hernandez[7] addressed a thick rod with point scatterers in two dimensions; finding that both enhanced diffusion and glassy regimes were accessible. In attempting to generalize to higher dimensions, however, we found that the order parameter n^* is no longer satisfactory.

In Sec. 3.2, we summarize the LG model for a rod diffusing through spheres, the structure of its transport coefficients, and the order parameters that have been used to characterize it. The framework and parameters of our simulations are presented in Sec. 3.3. We report the simulation data in Sec. 3.4, and introduce a correction to the order parameter to correct for the differences in the mean free path that we found in three dimensions rather than two. This, in turn, leads to a hypothesis for a useful order parameter in three dimensions which is a central result of this article.

3.2 Theory

3.2.1 The LG Model

The LG model in this work consists of a mobile tracer and a sea of immovable scatterers. The tracer moves ballistically between scatterers until it comes into contact with a scatterer and experiences a hard collision. Over time, the tracer experiences diffusive motion through the scatterer background, giving rise to a well-defined diffusion constant.

The tracer is described by a cylinder of length L and radius σ_t with end caps made of hemispheres of the same radius σ_t. It has a total mass M and uniform density. The scatterers are a sea of immobile spherical particles with radius σ_s. They are placed randomly in the box at homogeneous density ρ, and are allowed to overlap. The tracer dynamics is either that of ballistic motion between collisions or hard elastic collision upon contact with a scatterer. In the simulations, a finite size D-dimensional box with sides of length L_{box} satisfying periodic boundary conditions is used to represent the infinite extent of the formal system. Simulations with varying L_{box} confirmed that there were no finite size effects.

The tracer is placed in a random position and orientation within the periodic box. If that selection overlaps with a scatterer, the tracer is removed and placed randomly again. After 10,000 attempts to find a non-overlapped position, the scatterer background was re-created, and the iteration to place the tracer was re-initiated. Such reboots of the scatterer positions were rarely needed to find an initial tracer position even at the largest scatterer densities considered here.

The tracer is given a random translational and rotational velocity taken from independent Maxwellian distributions with temperature T. It can then be propagated by the classical equation of motion with the only interactions arising from the hard collisions—either head-on or glancing—between the rod and the scatterers.

3.2.2 Transport Coefficients

The transport coefficients for tracers diffusing across a random LG model

can be derived analytically in certain limiting cases. For a random scatterer background, the analytic form of the diffusion constant has been computed in 2D for the low density case.[3] Specifically, Moreno and Kob[3] obtained the low-density diffusion limit from kinetic theory and mode coupling theory for a 2D medium with point obstacles following approach similar to Ref..[14] They also added a correction factor for moderate densities, resulting in the reduced diffusion constant,

$$D_{\text{com}}/D^0_{\text{com}} = 1 + (32/9\pi)\rho^* \ln \rho^* \tag{3.1}$$

where

$$\begin{aligned} D_{\text{com}} &= \frac{3\langle v \rangle}{16\rho R} && (3.2) \\ p^* &= \rho R^2 && (3.3) \\ R &= (L_{\text{Kob}} + (\pi - 1)\sigma)/\pi && (3.4) \end{aligned}$$

In their model, the rigid rod was represented by N point-wise beads of mass m placed in a straight line with intervals spacings of 2σ. The length of the rigid rod is consequently described by $L_{\text{Kob}} \equiv 2(N-1)\sigma$. They set the size of their scatterers to zero without loss of generality by way of renormalizing the effective length of the rod as $R = (L_{\text{Kob}} + (\pi - 1)\sigma)/\pi$.

The model of Moreno and Kob can be mapped to the thick rod and LG scatterers discussed here through the following set of transformations:

$$L = L_{\text{Kob}} + \pi\sigma \tag{3.5}$$

$$n^* = \frac{\rho(L_{\text{Kob}} + \pi\sigma)}{\pi^2} \; , \tag{3.6}$$

where L and σ are the length and radius of the thick rod. Note that, unlike in our LG systems, their scatterers are not allowed to overlap. Our 2D results are compared to these theoretical values in Sec. 3.4, and the agreement is generally good at lower densities. The theory fails to have agreement at higher scatterer densities where both the differing nature of the scatterers and the excluded volume of the particle play an important role.

3.2.3 Order Parameters

In general, the reduced diffusion constant scales as

$$D_{\text{red}} \propto v\lambda \tag{3.7}$$

where v is the average velocity of the center of mass of the rod and λ is its mean free path obtained for sufficiently long trajectories.

The mean free path is inversely proportional to the product of the density of scatterers and the tracer-scatterer collision cross-section. For a 2D needle with length L moving though a sea of point scatterers, the mean free path is proportional to $\frac{1}{\rho L}$, where ρ is the density of scatterers. The cross-section is the length of the tracer. Insertion of the mean free path into Eq. 3.7 and division by vL results in a reduced diffusion constant which scales as

$$\begin{aligned} D_{\text{red}} &\propto \frac{1}{\rho L^2} && (3.8) \\ &\propto \frac{1}{n^*} && (3.9) \end{aligned}$$

This suggests that n^* is a good order parameter for the system in 2D.

In three dimensions, the situation is different. The mean free path of a needle with length L and thickness σ though a sea of point scatterers is given by $\frac{1}{\rho L \sigma}$ because the cross-section is proportional to the areas of the rectangle $L\sigma$. Applying the same transformations as before to obtain the reduced diffusion constant gives:

$$\begin{aligned} D_{\text{red}} &\propto \frac{1}{\rho L^2 \sigma} && (3.10) \\ &\propto \frac{1}{\frac{\sigma}{L} n^*} && (3.11) \end{aligned}$$

This implies that $\frac{\sigma}{L} n^*$ would make a good order parameter for 3D. We take the ratio $\frac{\sigma}{L}$ to be a correction factor γ on the reduced diffusion n^* to create a new order parameter: γn^*. We show in Sec. 3.4 that this new order parameter provides the desired invariance in our test simulations.

3.3 Numerical Methods

3.3.1 Numerical Integration and Propagation

The integration algorithm for the evolution of the tracer under the classical equation of motions is simplified by the fact that the motion is ballistic as long as there is no collision.

The algorithm used here is time-step based, evolving the system forward in time in successive steps at constant velocity and correcting those steps which involved a scatterer-tracer collision through a careful accounting of the collision event.[7,8] Even at the highest densities explored in this work, the frequency of these collisions, relative to our time step, were sufficiently low that the calculations could be performed in reasonable time.

Although an event-driven molecular dynamics integrator can be more efficient then a time step based integrator,[24] we want to be able to sample data at shorter time scales then the collision time scale; and, as such need discrete time steps independent from the collision rate. Once a collision has been detected, the tracer's motion is reversed until it has reached the point of contact, where the equations for a hard collision are applied. After a set amount of time the position and velocity of the tracer is recorded for data collection and analysis. After a set number of time steps, which corresponds to a given amount of real time, another scatterer background is generated, the tracer's position and velocity is regenerated, and a new trajectory is started. After all of the trajectories are complete, the relevant correlation functions are calculated and the transport coefficients are extracted. The numerical integration of trajectories and averaging of the correlation functions are done with in-house Fortran code; the fitting and plotting with in-house Python code.

Each of the trajectories reported here were integrated on the first-generation XSEDE Stampede CPU nodes (2.7 GHz Xeon E5-2680 8-core Sandy Bridge processors with the Intel Xeon Phi SE10P KNC MIC coprocessor), and completed on one core in less then 24 hours of processing and analysis time.

3.3.2 Algorithms for Determining Transport Coefficients

The translational diffusion constant D_{com} is extracted via three different methods: (i) using a linear fit of the long time mean square displacement (MSD)

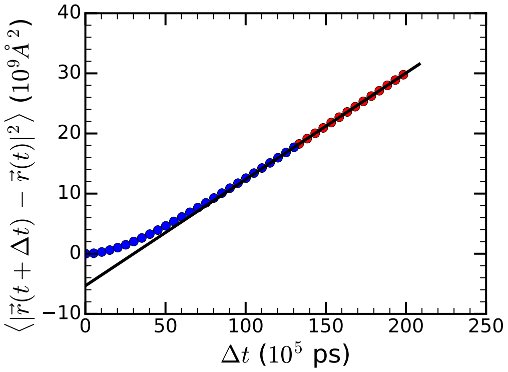

Figure 3.1: A typical MSD (blue and red dots) for a 2D simulation as a function of displacement time Δt. Specifically, the parameters are: $n^* = 0.1$, $L = 14.142$ Å, $\sigma_s = 0.5$ Å, $\sigma_t = 0.5$ Å. The blue points are those excluded from the fitting due to not being in the linear regime. The black line is the linear fit of the red points with a slope of 1769.02 ± 0.24 ps.

as illustrated in Fig. 3.1 for a particular set of parameters, (ii) using a two variable power law fit of the long time MSD, and (iii) through integration of the velocity autocorrelation function.

In the first and second method, we take advantage of the relationship between the diffusion constant and the MSD given by the Brown-Einstein-Smolouchowski relation,

$$D_{\text{com}} = \frac{1}{2D} \lim_{\Delta t \to \infty} \frac{d}{d(\Delta t)} \langle (\vec{r}(t+\Delta t) - \vec{r}(t))^2 \rangle_t \tag{3.12}$$

where D is the dimensionality of the system. Note that $\langle ... \rangle_t$ is an average over all time t. The use of Δt for several prior t's instead of the fixed starting point at $t = 0$ allows for enhanced averaging.

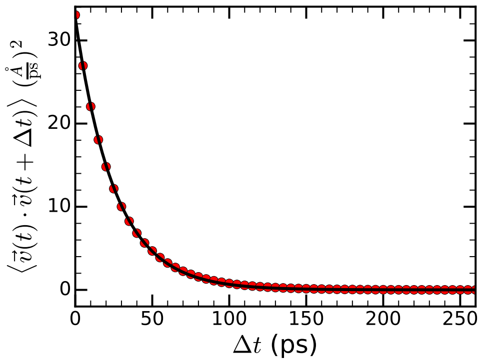

Figure 3.2: A typical velocity autocorrelation function (red dots) for a 2D simulation as a function of displacement time Δt at the same parameters as figure 3.1. The black line is the exponential fit with a decay time of 25.615 ± 0.009 ps.

D_{com} can then be extracted numerically from the mean-square displacement. In the first method, we fit the long time MSD to a line whose slope is $2DD_{\mathrm{com}}$. In the second method, we account for the possibility that the finite size of the data can cause convergence errors leading to apparent anomalous diffusion. The corresponding assumption of a power law form —with m and α as the prefactor and exponent, respectively— for the position correlation function in Eq. 4.11 leads to an intermediate time approximation of the diffusion constant,

$$D_{\mathrm{com}} = \frac{1}{2D}\,\frac{d}{d\Delta t}(m\,\Delta t^{\alpha})\Big|_{\Delta t\approx t^*} \tag{3.13}$$

where t^* is a characteristic time associated with the intermediate region where the power law is fit to the data, and we approximate it as the median of the times in the fitting window.

After simple algebra, we find that the diffusion constant is

$$D_{\mathrm{com}} \approx D_{\alpha}(t^{*})^{\alpha-1} \tag{3.14}$$

where $D_{\alpha} \equiv \frac{\alpha m}{2D}$. For a Brownian (or any nonanomalous) system, as $t^{*} \to \infty$ then $\alpha \to 1$. Consequently, Eq. 4.13 reduces to $D_{\mathrm{com}} = D_{\alpha}$, which is the expected limiting behavior.

A typical fit of the velocity autocorrelation data is shown in Fig. 3.2. The relationship between the velocity autocorrelation function (VAC) and D_{com} is given by the following Green-Kubo relation:

$$D_{\mathrm{com}} = \frac{1}{D}\int_{0}^{\infty} \langle \vec{v}(t+\Delta t)\vec{v}(t)\rangle_{t}\mathbf{d}(\Delta t) \tag{3.15}$$

where D is the dimensionality of the system. The use of the integrand as an average over t for each given Δt is not formally necessary, but it is numerically useful as it allows for more points to contribute to the numerical integral.

3.3.3 Numerics in Determination of Diffusion Coefficients

The diffusion constant can be obtained from numerically determined MSDs such as that shown in Fig. 3.1. At intermediate times —beyond the initial inertial regime and before the end of the trajectories,— the system exhibits diffusive behavior and satisfies a form linear in time. $\left\langle (\vec{r}(t+\Delta t) - \vec{r}(t))^2 \right\rangle \approx v_0 \Delta t$. Insertion into Eq. 4.11 yields the diffusion constant,

$$D_{\text{com}} = \frac{v_0}{2D} \tag{3.16}$$

For example, the slope v_0 of the MSD in Fig. 3.1 is 1769.0 ± 0.2 Å/ps. Consequently, the diffusion rate obtained from the linear MSD plot is 442.25 ± 0.06 $\frac{2}{ps}$.

Alternatively, the fits can be performed on a log-log representation of the data. From the data shown in Fig. 3.1, such a log-log fit led to the optimized parameters: t^* = 1.67 μs, α = 1.230 ± 0.006, and D_α = 16.6 $\frac{2}{ps}\frac{1}{ps^\alpha}$. Use of Eq. 4.13 yields the diffusion constant, D_{com} = 444.66 ± 39.0 $\frac{2}{ps}$. Note that these error bars are much larger than the error for the linear fit, since the linear fit assumes the exponent α is exactly 1, so error in the determination of this exponent is not propagated.

Alternatively, the diffusion constant can be obtained from the VAC function.

We approximate it as a single exponential $\langle v^2 \rangle e^{-t/\tau}$ where τ is the decay time. The diffusion constant of Eq. 4.14 then reduces to:

$$D_{\text{com}} = \frac{\langle v^2 \rangle}{D v_0} = \frac{2kT\tau}{Dm} \tag{3.17}$$

The values of the fitting parameters for the same case as in Fig. 3.1 are: $\langle v^2 \rangle$ = 32.680 ± 0.008, and τ = 25.615 ± 0.009 with the effective dimensionality of the system set to 2. As such, one recovers a diffusion constant equal to 418.54 ± 0.04 $\frac{2}{ps}$.

The values of the diffusion constants obtained from the linear MSD and VAC fits are much larger than the width of the error bars. However, the diffusion constant obtained from the VAC is on the order of the error seen in the log MSD fit. This is due to the linear MSD and VAC error calculations not accounting for convergence error. We take the variance for all of our averages when computing the MSDs and VAC. We then use these variances to judge the error in the fit for the MSD and VAC fitting. This method works well for estimating noise in the fitting itself. However, to compute the diffusion exactly, we would need to take averages at infinitely long time with infinitely fast velocity sampling. Since our samples are of finite size, there is convergence error in the diffusion constant that is not represented in the variance of the individual data points in the linear MSD and VAC. An illustration of the convergence with increasing number of scatterers is shown in Fig. 3.3 for two

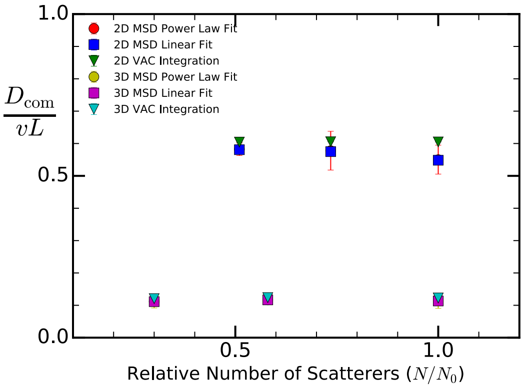

Figure 3.3: The 2D and 3D diffusion constants obtained on a periodic box with increasing size and corresponding increasing number of scatterers. The tracer length is held fixed at $L = 31.623$ Å and 21.544 Å in 2D and 3D, respectively. The number of scatterers in the largest finite box is N_0 equal to 1960 and 3375 in 2D and 3D, respectively. In all cases, the box size and N satisfy the condition that the scatterer density is 0.001, and $n^* = 1.0$.

representative cases in 2D and 3D. We thus extract the diffusion constant via the three approaches in order to obtain an estimate of the relative accuracy of the numbers in a way that would not be represented by the apparent convergence of a given approach, and report the numbers accordingly.

3.4 Results

3.4.1 Tracer in Two Dimensions

The reduced diffusion constant at constant n^* for three different n^* and three different cases of the characteristic lengths L_0 of the diffusing rod is shown

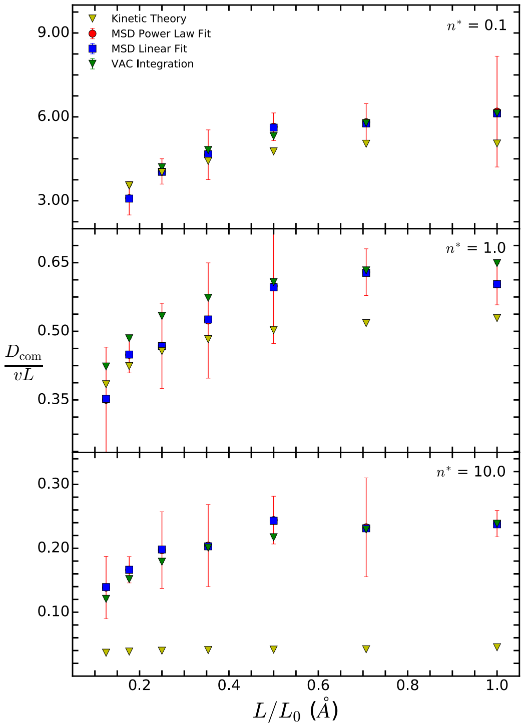

Figure 3.4: The 2D reduced diffusion constant as a function of tracer length at three different constant values of n^* scaled by a characteristic length L_0 = 28.3, 63.2 and 200 Å in each panel from top to bottom, respectively. Notice that the reduced diffusion is a good order parameter at large tracer length (low density at constant n^*) because the curves are flat in this region, and hence D_{com} is a constant with respect to L.

in Fig.3.4. The values L_0, noted in the figure caption, are characteristic in the sense that they represent the regime (at sufficiently large lengths) when the diffusion constant has plateaued for each given n^*.

The observed reduced diffusion at constant n^* exhibits similar behavior over a wide range of densities, including in the enhanced diffusion regime. In particular, they exhibit a horizontal asymptote for values with a constant diffusion constant at large tracer length. This is consistent with the hypothesis that n^* is a good order parameter for the system in this regime, since the reduced diffusion is a function of n^* alone.

However, n^* is not a good order parameter at low L as indicated by the depression in the curve towards zero at zero L. At constant n^*, a decrease in L implies an increase in number density, but a decrease in collision cross section such that the overall reduced diffusion in unchanged. For a system with space filling rods and scatterers, L is not the only variable that determines the cross section. At zero L, the tracer is a sphere of radius σ_t, surrounded by spheres of radius σ_s. In this limit, the diffusion goes to zero. To fix this, σ_t and σ_s must change to hold the cross section constant as L decreases. We create a new effective L such that:

$$L_{\text{eff}} = L + 2\sigma_s + 2\sigma_t \tag{3.18}$$

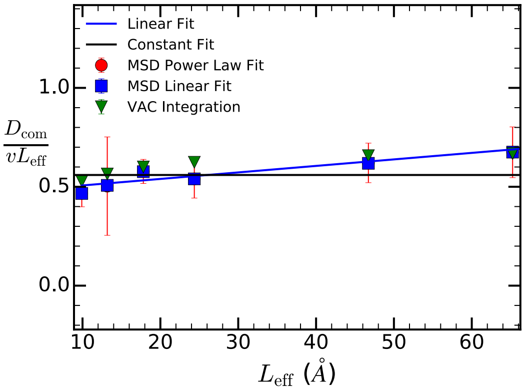

Figure 3.5: The dependence of the 2D translational diffusion constant of the tracer on the effective length L_{eff} at constant n^*_{eff}. In this case $n^*_{\mathrm{eff}} = 1.0$, $\sigma_s = \sigma_t = 0.5$ Å. The blue line is the linear fit, and the black line is a constant fit. The constant fit is within the error bars of the power law fit, $\frac{D_{\mathrm{com}}}{vL_{\mathrm{eff}}} \sim .003\ L_{\mathrm{eff}}$, which is within 1.5 σ from zero.

and from this create an effective n^*:

$$n^*_{\mathrm{eff}} = \rho L^D_{\mathrm{eff}} \tag{3.19}$$

As shown in Fig. 3.5, This n^*_{eff} is a good order parameter in 2D, as it correctly accounts for the cross section of the tracer when it is not dominated by L alone.

3.4.2 Tracer in Three Dimensions

The reduced diffusion constant in 3D for three values of n^* is plotted in Fig. 3.6. The L_0 values refer to the largest lengths of the tracer considered here for three-dimensional scatterers at a particular n^*. Their values were chosen

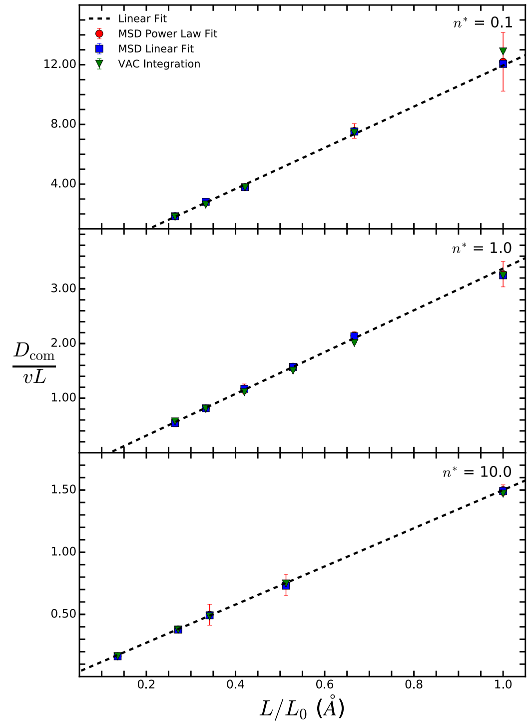

Figure 3.6: The 3D reduced diffusion constant as a function of tracer length at constant values of n^* — as also displayed for the 2D case in figure 3.4 — scaled by a characteristic length L_0 = 7.0, 29.2, 63.0 Å from top to bottom, respectively. The dashed line is a linear fit to the data, with R^2 values > 0.999 for all plots. Note that the reduced diffusion is nowhere a good order parameter in 3D.

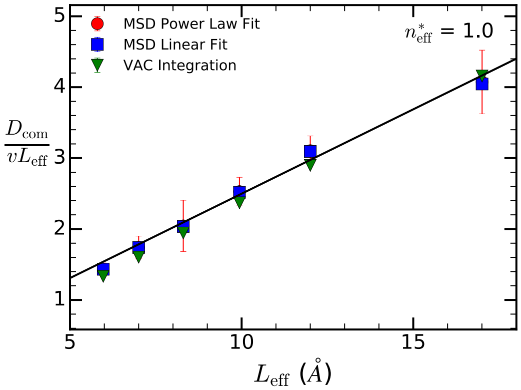

Figure 3.7: The 3D translational diffusion constant of the tracer as a function of the effective tracer length L_{eff} at constant n^*_{eff}. The parameters are n^*_{eff} = 1.0, $\sigma_s = \sigma_t = 0.5$ Å. The black line is the linear fit, $\frac{D_{\text{com}}}{vL_{\text{eff}}} \sim .24\ L_{\text{eff}}$, with a slope that is about 100 times that in the 2D case.

to correspond to the two dimensional cases of the previous subsection.

The most obvious difference to the trends seen in 2D is that there is only one regime, and it is linear. This implies that in three dimensions, n^* is not a good order parameter in any limit because it cannot uniquely predict the diffusion constant. Correcting for excluded volume does not help the situation either. When the excluded volume is accounted for, the diffusion is still a strong function of the scatterer length at constant n^*_{eff}, as shown in Fig. 3.7.

A simple fix would be to attempt to find a length scale that is proportional to L. However, this would not lead to a flat curve. The linearity could only be reduced to a constant via division by L if the y-intercept of the linear fit were zero. This is not the case for any of the n^* observed.

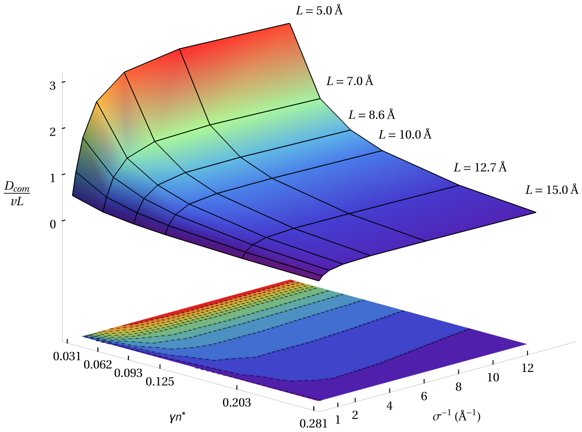

Figure 3.8: The 3D reduced diffusion constant is displayed as a contour and the 3D-surface plots over the two-dimensional domain of γn^* and scatterer and tracer radius σ^{-1}. The black lines on the surface indicate constant L as indicated, and also correspond to the values of γn^* on the bottom left axis. The vertices of the lines on the upper surface are explicitly computed to which the surface has been fitted. The dashed contour lines represent lines of constant reduced diffusion and potential order parameters.

3.5 Discussion

A new order parameter γn^* for the diffusion of rods through scatterers in three dimensions was constructed in Sec. 3.2. The need for this scaling law lies in its use to surmise and predict the behavior of these systems with a minimum number of characteristic degrees of freedom in the parameter space. These considerations, and their relevance to experiment, are our primary motivation for its construction and elaboration.

To numerically confirm that γn^* is indeed a good order parameter, the diffusion constant was determined or various values of L, σ, and ρ and summarized in Fig. 3.8. A surface was extrapolated over the set of resultant reduced diffusion points.

The surface is indeed nearly constant over domains with constant values of γn^* suggesting that this quantity is a good order parameter across most of these three-dimensional systems. These models are applicable to the classical diffusion of rod-like molecules on surfaces. For example, Fichthorn and coworkers

found that the dynamics of dimers on medal surfaces can be complex and highly dependent on the relative shape and size of the dimer and geometry of the underlying surface.[25–27] While the present work does not explicitly consider inhomogeneities due to an underlying surface in the 2D case, it does consider the inhomogeneities in the plane of the surface are represented by the scatterers. Perhaps not surprisingly, we found similar complexity, but have added the possibility of corresponding behavior as captured though the scaling law.

The diffusion of a rod in an environment with controlled scatterer density is experimentally realizable, and its existence has motivated, in part, much of the work by other groups and us. For instance, Roichman et al[28] follow the dynamics of a single silver nanowire confined to two dimensions as it diffuses through a set of randomly generated repelling focused laser beams or polymer pillars. Their rods experience viscous and hydrodynamic effects that are not included in the simple models of this work. Indeed, these effects lead to a breakdown of the scaling laws that we have found here, thereby illustrating the need for including such effects.

Similarly, Composto and coworkers[29] observed the diffusion of a titanium dioxide nanorod though a polystyrene melt where the length and thickness of the nanorod is comparable to the radius of gyration of the polymer melt. They found that the translational diffusion of the nanorod can be up to three orders of magnitude faster than what would be expected from a uniformly distributed environment in which the rod diameter is smaller than the entanglement mesh size. Recognizing that their nanorods are constrained by the polymer in a similar way to how our rods are constrained by scatterers, this is evidence for the enhanced diffusion our group[7] observed earlier. Moreover the 3 dimensional nature of the confinement of the polymer network allows for enhanced diffusion to persist even in three dimensions when a disconnected network of scatterers does not lead to it.[8] Once again, this analysis is clearer because of the differences observed in systems with putative corresponding order parameters that break down because of the additional complexities of the actually system. Thus, the current findings afford us a new way to better characterize the nonadditive effects that emerge from increased complexity in the diffusing medium or the scatterer network.

Finally, the scatterers in this work were arranged in the periodic box using a homogeneous random selection that permits naive overlaps. One possible concern is how a different selection of the scatterers would affect the results and the associated scaling law. The placement of the scatterers clearly presents the possibility for different dynamics. For example, if the scatterers were so heterogeneously placed so as to leave large and simply connected regions free of scatterers, the rod would diffuse ballistically within said regions deterred only slightly by a search through the interconnections, and thus diffuse faster. The scaling behavior found here may still be relevant in selected regimes, but proving this would require additional effort beyond the scope of this work.

In this article, we have determined how the reduced diffusion constants for a particle moving through an isotropic random LG scatterers differ between two and three dimensions. We have summarized the features necessary for identifying good order parameters as previously used to describe related systems, and obtained the corresponding order parameters for a spherocylinder solvated in a Lorentz gas of spherical particles. In two dimensions, the reduced density makes a good order parameter so long as excluded volume is properly accounted for. However, in three dimensions, the naive extension of the two-dimensional order parameter is insufficient to characterize the system. An approach accounting for excluded volume effects does not lead to an appropriate order parameter with invariant properties. We found that this is due to the failure of the two-dimensional order parameter to include the effects of the changes in the mean free path of the tracer in three dimensions. We derived and benchmarked the corrected 3D order parameter by extending the 2D order parameter using the correct scaling behavior of the mean free path with dimensionality.

The existence of an appropriate order parameter for these systems in two and three dimensions does more than provide a reduced variable with which to characterize them. It also suggests a mechanism by which the cylindrical tracer generally diffuses through the scatterers. In two dimensions, the motion of the rod tangentially to its parallel axis is confined by its length L whereas in 3 dimensions a small perturbation above or below the scatterer allows it to go freely past a would-be scatterer. Such different physics results in the rather different order parameters that we have observed here for two- and three-dimensions.

References

(1) Schmucker, A. L.; Harris, N.; Banholzer, M. J.; Blaber, M. G.; Osberg, K. D.; Schatz, G. C.; Mirkin, C. A. *ACS Nano* **2011**, *4*, 5453–5463.

(2) Hoener, B. S.; Byers, C. P.; Heiderscheit, T. S.; Indrasekara, A. S.D. S.; Hoggard, A.; Chang, W.-S.; Link, S.; Landes, C. F. *J. Phys. Chem. C* **2016**, *120*, 20604–20612.

(3) Moreno, A. J.; Kob, W. *Europhys. Lett.* **2004**, *67*, 820–826.

(4) Moreno, A. J.; Kob, W. *J. Chem. Phys.* **2004**, *121*, 380–386.

(5) Höfling, F.; Franosch, T. *Phys. Rev. Lett.* **2007**, *98*, 140601.

(6) Höfling, F.; Frey, E.; Franosch, T. *Phys. Rev. Lett.* **2008**, *101*, 120605.

(7) Tucker, A. K.; Hernandez, R. *J. Phys. Chem. B* **2010**, *114*, 9628–9634.

(8) Tucker, A. K.; Hernandez, R. *J. Phys. Chem. B* **2011**, *115*, 4412–4418.

(9) Lorentz, H. A. *Proc. R. Amst. Acad.* **1905**, *7*, 438–453.

(10) Gallavotti, G. *Phys. Rev.* **1969**, *185*, 308–322.

(11) Dettmann, C. P. *Commun. Theor. Phys.* **2014**, *62*, 521–540.

(12) Van Leeuwen, J. M. J.; Weijland, A. *Physica* **1967**, *36*, 457–490.

(13) Zwanzig, R. *Phys. Rev.* **1963**, *129*, 486–495.

(14) Götze, W.; Leutheusser, E.; Yip, S. *Phys. Rev. A* **1981**, *24*, 1008–1015.

(15) Bruin, C. *Physica* **1974**, *72*, 261–286.

(16) Tucker, A. K.; Hernandez, R. *J. Phys. Chem. B* **2012**, *116*, 1328–1334.

(17) Khalilian, H.; Fazli, H. *J. Chem. Phys.* **2016**, *145*, 164909.

(18) Zeitz, M.; Wolff, K.; Stark, H. *Eur. Phys. J. E* **2017**, *40*, 23–33.

(19) Mallory, S. A.; Valeriani, C.; Cacciuto, A. *Phys. Rev. E* **2014**, *90*, 032309.

(20) Tung, C.; Harder, J.; Valeriani, C.; Cacciuto, A. *Soft Matter* **2016**, *12*, 555–561.

(21) Frenkel, D.; Maguire, J. F. *Phys. Rev. Lett.* **1981**, *47*, 1025–1028.

(22) Munk, T.; Höfling, F.; Franosch, T. *Europhys. Lett.* **2009**, *85*, 30003.

(23) Leitmann, S.; Höfling, F.; Franosch, T. *Phys. Rev. E* **2017**, *96*, 012118.

(24) Bannerman, M. N.; Sargant, R.; Lue, L. *J. Comput. Chem.* **2011**, *32*, 3329–3338.

(25) Wang, R.; Fichthorn, K. A. *Phys. Rev. B* **1993**, *48*, 18288–18291.

(26) Wang, J.-C.; Fichthorn, K. A. *Langmuir* **1996**, *12*, 139–144.

(27) Ramirez-Pastor, A.; Nazzarro, M.; Riccardo, J.; Pereyra, V. *Surf. Sci.* **1997**, *391*, 267–277.

(28) Kasimov, D.; Admon, T.; Roichman, Y. *Phys. Rev. E* **2016**, *93*, 050602.

(29) Choi, J.; Cargnello, M.; Murray, C. B.; Clarke, N.; Winey, K. I.; Composto, R. J. *ACS Macro Lett.* **2015**, *4 (9)*, 952–956.

Chapter 4

Molecular dynamics of a mixed solvent system: diffusion anomalies and coarse graining

4.1 Introduction

In the real world, chemical reactions do not often happen in isolated beakers. Any living organism is a complex crowded soup of chemical, biochemical and physical reactions. However, in the lab, reactions are often assumed to be happening in dilute, isolated solutions. The effects of this molecular crowding have been explored in many specific contexts.[1–3] Crowded environments have been implicated in causing anomalous diffusion in cellular and protein environments.[4–6] Theoretically, anomalous diffusion can be attributed to the generator of motion approximating a continuous time random walk instead of a discrete time one, implying a fractional diffusion equation.[7] The question remains: how do crowded environments generate these dynamics? In this work, we focus on a simplified model of a complex crowded system: a shaped tracer in a sea of Lorentz scatterers with a Langevin solvent.

For a particle in a crowded system, the solvent is a multi-scale mixture of many simple solvents. We model this as a combination of a hard sphere solvent, representing large, slow-moving molecular structures and an implicit light solvent generating Langevin dynamics. We study how the combination of a static structure generating excluded volume and a softer Langevin friction mix as the system approaches the glassy regime. In particular we are interested in how a spherocylindrical tracer diffuses through this mixture of solvents compared to a single hard sphere or Langevin solvent. How do these solvents approximate each other? Can a mixture of solvents generate crowding behavior?

We introduced the requirement for dynamical consistency[8,9] in our previous work. Dynamical consistency reflects the observation that dynamical systems are not only a function of space, but of time. Coarse grained matching of spatial structures without matching the appropriate timescales generates errors. This addresses the dynamical consistency between explicit excluded volume solvents such as the Lorentz gas and implicit solvents such as the Langevin solvent.

4.2 Theory

4.2.1 Order Parameters

For a spherocylinder moving through a sea of spherical scatterers, the order parameter that fully identifies the reduced diffusion coefficient is dependant on the dimensionality. For a two dimensional system with no excluded volume, the order parameter is n^*

$$n^* = \rho L^2 \tag{4.1}$$

where ρ is the scatterer density and L is the tracer length. For a system with needles and scatterers with thickness σ_{T} and σ_{S} respectively, this equation can be extended to

$$n^*_{\mathrm{ex}} = \rho (L_{\mathrm{eff}})^2 \tag{4.2}$$

where $L_{\mathrm{eff}} = L + 2\sigma_{\mathrm{T}} + 2\sigma_{\mathrm{S}}$. n^* was properly extended to three dimensions in our previous work.**hern18i** The three dimensional version of n^*, in this work called κn^* is defined as

$$\kappa n^* = \rho L_{\mathrm{eff}}^2 (\sigma_S + \sigma_T) \tag{4.3}$$

These order parameters have the property that the reduced translational tracer diffusion $\frac{D}{vL}$, where v is the average tracer velocity, is only a function of the order parameter. This allows the order parameter to fully define the solvent regime the tracer is experiencing.

4.3 Numerical Methods

4.3.1 Numerical Integration and Propagation

We integrate the equations of motion for the spherocylinder tracer using classical equations of motion with a time-step based integrator with characteristic step time t_{step}.

There are two parts to the integrator, the hard core collision algorithm, and the Langevin solvent implementation. The hard core collision algorithm updates the velocity of the tracer after a hard collision with a static solvent particle using the exact equation for the impulse of hard collision between a mobile and stationary object.[10,11]

$$j = \frac{-2\vec{v} \cdot \hat{n}}{(m^{-1}) + [I^{-1}(\vec{r_{\text{p}}} \times \hat{n})] \cdot \hat{n}} \tag{4.4}$$

where j is the magnitude of the impulse, $\vec{v}$ is the current tracer velocity, $\hat{n}$ is the normal vector of the collision, I is the moment of inertia of the tracer and

r_p is the point of contact. The post collisional velocities are:

$$\vec{v}_\mathrm{f} = \vec{v}_\mathrm{i} + \frac{j}{m}\hat{n} \tag{4.5}$$

$$\vec{\omega}_\mathrm{f} = \vec{\omega}_\mathrm{i} + I^{-1}(\vec{r}_\mathrm{p} \times j\hat{n}) \tag{4.6}$$

Collisions are elastic, instantaneous, and frictionless. There is a no-slip condition that prevents the tracer from rotating co-linearly with its length, which is denoted the x direction in the frame of the tracer. This no-slip condition applies to the random force as well, where it is assumed that the x component of the moment of inertia, I_{xx} is infinite.

Each time step is broken up into three parts. First, the tracer is moved forward ballistically using Velocity-Verlet, which in the absence of a potential is exact. Next, overlaps between the tracer and scatterers are checked for and, if found, the system is rewound to the point of impact and equation 4.4 is applied. The system is then propagated to the end of time step and checked for overlaps again. This process is repeated until the tracer reaches the end of the time step with no scatterer overlaps. Finally, the Langevin dynamics are updated. The friction is applied to the translational and rotational modes and the random forces are applied to the tracer using the following equations.

$$\xi_{\mathrm{T}} = \sqrt{\frac{k_{\mathrm{B}}T}{m}(1 - e^{-2\gamma_{\mathrm{T}} t_{\mathrm{step}}})} \tag{4.7}$$

$$\xi_{\omega} = \sqrt{\frac{k_{\mathrm{B}}T}{I_{\mathrm{yy}}}(1 - e^{-2\gamma_{\omega} t_{\mathrm{step}}})} \tag{4.8}$$

The complete equation for updating the tracer translational and rotational velocity is given by:

$$\vec{v}(t + t_{\mathrm{step}}) = \left[\vec{v}(t) + \sum_i \frac{j_i}{m}\hat{n}_i\right] e^{-\gamma_{\mathrm{T}} t_{\mathrm{step}}} + \hat{G}(t)\xi_{\mathrm{T}} \tag{4.9}$$

$$\vec{\omega}(t + t_{\mathrm{step}}) = \left[\vec{\omega}(t) + \sum_i I^{-1}(r_{\mathrm{p}_i} \times j_i\hat{n}_i)\right] e^{-\gamma_{\omega} t_{\mathrm{step}}} + \hat{G}(t)\xi_{\omega} \tag{4.10}$$

where m is the mass, I is the moment of inertia perpendicular to the length of the tracer, ξ_{T} and ξ_{ω} represent the magnitude of the random force and $\hat{G}(t)$ is a Gaussian-distributed memoryless unit vector chosen randomly for each time step. γ_{T} and γ_{ω} are the translational and rotational frictions, respectively; j_i, $\hat{n}_i$, and r_{p_i} are the impulse, normal vector, and point of contact of the i^{th} collision that occurred between t and $t + t_{\mathrm{step}}$, see equation 4.4.

After a set amount of time, the tracer's information is recorded for analysis.

After each trajectory has completed its run time, the tracer and scatterer background are regenerated to create a new trajectory. Note that the scatterers are placed randomly at the beginning of the simulation and are allowed to overlap. Each trajectory lasted 200,000 ps with data being recorded every $0.1ps$. Around 550 trajectories were calculated for each data point studied here.

Each of the trajectories reported here were integrated on XSEDE Bridges CPU nodes (2.3 - 3.3 GHz Intel Haswell (E5-2695 v3) 14 core CPUs) and completed on one core in less then 24 hours.

4.3.2 Algorithms for Determining Transport Coefficients

4.3.2.1 Translational Diffusion

The translational center-of-mass diffusion coefficient D_{com} is extracted using three complimentary methods. First, the diffusion coefficient is extracted from a linear fit of the long time mean square displacement using the standard Brown-Einstein-Smolouchowski relation, see equation 4.11

$$D_{\text{com}} = \frac{1}{2D} \lim_{\Delta t \to \infty} \frac{d}{d(\Delta t)} \langle (\vec{r}(t+\Delta t) - \vec{r}(t))^2 \rangle_t \tag{4.11}$$

where D is the system dimensionality and $\langle ... \rangle_t$ represents and average over all time.

However, high density systems with significant excluded volume experience subdiffusion, where the power of t in the long time limit does not converge to one, but instead to t^α where α is the anomalous diffusion exponent. This anomalous subdiffusion is closely related to the trapping that results from the large excluded volume generated by randomly place scatterers.[12,13]

In order to observe the value of α directly, we plot the MSD on a log-log plot and fit the long time regime to a linear function $\log MSD(t) = mx + b$. Assuming the underlying MSD has a power law form, the anomalous diffusion coefficient D_α is the intercept and the anomalous exponent is the linear prefactor. Converting D_α to D_{com} is not trivial as the units of the anomalous diffusion coefficient are not the same as the units of the regular diffusion coefficient. To convert to the linear coefficient, we find the characteristic time associated with the finite region we have averaged, called t^*. We approximate t^* by taking the median of the times averaged in the fitting window.

$$D_{\text{com}} = \frac{1}{2D} \frac{d}{d\Delta t}(m\,\Delta t^\alpha)\bigg|_{\Delta t \approx t^*} \tag{4.12}$$

The diffusion can then be expressed as a function of D_α and t^* as shown in

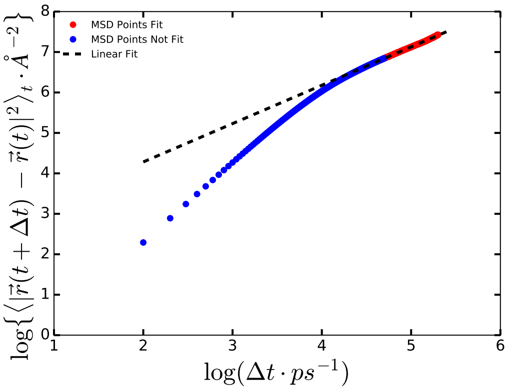

Figure 4.1: Typical MSD Fit on a log-log plot, allowing the fit of the diffusion exponent as well as the diffusion coefficient to be extracted. The red points indicate the long time regime, whereas the blue points indicate the short to medium regime. The dashed line is the fit. Taken from a 2D system of hard spheres with $n^*_{\mathrm{ex}} = 1.0$

equation 4.13.

$$D_{\mathrm{com}} \approx D_\alpha (t^*)^{\alpha-1} \tag{4.13}$$

In the limit of a Brownian system, $t^* \to \infty$ and $\alpha \to 1$. Consequently, Eq. 4.13 reduces to $D_{\mathrm{com}} = D_\alpha$, which is the correct limit.

Finally, we extract D_{com} from the velocity autocorrelation function (VAC) using the Green-Kubo relation shown in equation 4.14.[14]

$$D_{\mathrm{com}} = \frac{1}{D}\int_0^\infty \langle \vec{v}(t+\Delta t)\vec{v}(t)\rangle_t \mathbf{d}(\Delta t) \tag{4.14}$$

where D is the dimensionality and $\langle \vec{v}(t+\Delta t)\vec{v}(t)\rangle_t$ is the velocity autocorrelation function (VAC). To maximise the number of data points that contribute to the numeric integral we average over all t as well as integrating over Δt,

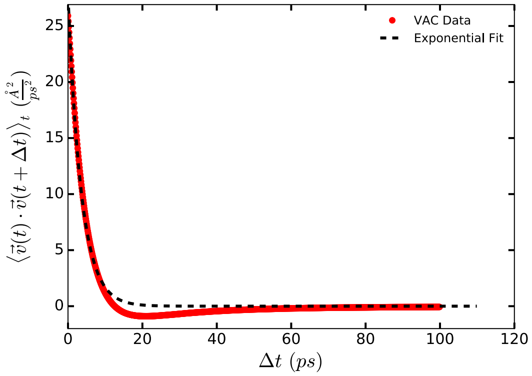

Figure 4.2: Typical VAC (red) and corresponding exponential fit (dashed line). The diffusion is extracted from quadrature integration of the red points, while the effective friction is extracted from the exponential fit using equation 4.15. Notice the negative anti-correlation VAC regime that is characteristic of a dense hard sphere system. This regime cannot be approximated by a Langevin solvent and is the reason the Langevin solvent is increasingly inaccurate at representing hard dynamics at high density. Taken from a 2D system of hard spheres with $n^*_{\text{ex}} = 1.0$

taking every possible t as our starting point and averaging them.

The VAC can also be used to extract an effective translational friction for a hard sphere system by fitting to the following exponential decay. Note that for a dense system, the VAC has a large negative tail that cannot be replicated by a Langevin system, as the anti-correlation is due to rattling in a confined space.

$$\frac{\langle \vec{v}(t) \cdot \vec{v}(t+\Delta t) \rangle_t (\Delta t)}{\langle v^2 \rangle_t} = e^{-\gamma_{\text{eff}} \Delta t} \tag{4.15}$$

where γ_{eff} is the effective Langevin friction of the hard sphere background.

4.3.2.2 Rotational Diffusion

A rotational autocorrelation function (RAC) can be defined in a similar method to the definition of the VAC, see 4.14. However, extracting an analog of the diffusion coefficient is dependant on the strength of the friction. In the high friction limit, the Debye approximation can be used to show that[15]

$$C_\omega(\Delta t) \equiv \langle \hat{\mu}(t) \cdot \hat{\mu}(t+\Delta t) \rangle_t(\Delta t) \approx e^{2D_\mathrm{R}\Delta t} \tag{4.16}$$

where D_R is related to the rotational friction $D_\mathrm{R} = \frac{k_\mathrm{B}T}{I\gamma_\omega}$ and $\hat{\mu}$ is a unit vector parallel to the length of the rod. The intermediate friction regime is more complex, given by[16]

$$C_\omega(\Delta t) = e^{-\frac{D_\mathrm{R}}{\gamma_\omega}(\gamma_\omega \Delta t + e^{-\gamma_\omega \Delta t} - 1)} \tag{4.17}$$

Note that in the low friction limit,

$$\lim_{\gamma_\omega \to 0} C_\omega(\Delta t) \to \frac{k_\mathrm{B}T}{2I}\Delta t$$

which is independent of friction. This makes numerically extracting the rotational diffusion coefficient for a system with weak friction very difficult, as the difference between small frictions becomes undetectable from zero.

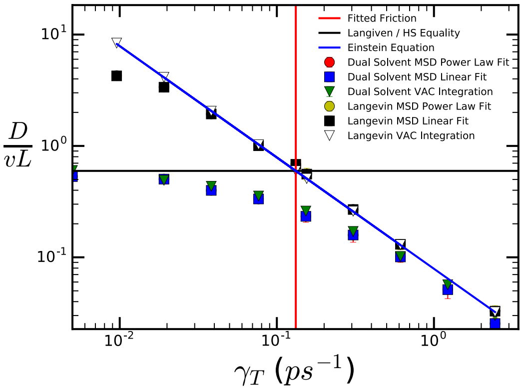

Figure 4.3: This plot shows the interaction of the dual Langevin-Lorentz solvent compared to the pure Langevin solvent as a function of translational friction. The red line is the friction which corresponds to the pure 2D Lorentz gas solvent with $n^* = 1.0$. The black line is to show that there is a correspondence between the Lorentz solvent and a Lanvegin solvent using the same effective friction. The blue line is the theoretical result from the Einstein equation for a Langevin system with that friction. The circles are MSD power law fits, the squares correspond to MSD linear fits, and the triangles correspond to VAC fits. This plot shows that at $n^* = 1.0$, the translational dynamics of the Langevin solvent are a good approximation to the Lorentz gas.

4.4 Results and Discussion

Figure 4.3 investigates what happens when the Langevin and Lorentz solvents are mixed in the same system. The Langevin solvent is a good match for the Lorentz gas at low densities, as expected due to lack of significant excluded volume acting as a differentiator. At low γ, the hard sphere solvent dominates. At intermediate γ, the γ_{eff} generated by the hard spheres and the explicit Langevin γ_{T} are additive. At high γ_{T}, the Langevin friction dominates.

Figure 4.4 explores how the Langevin solvent approximates the Lorentz gas over a large range of n^*_{ex}. At low density, the Langevin solvent is an

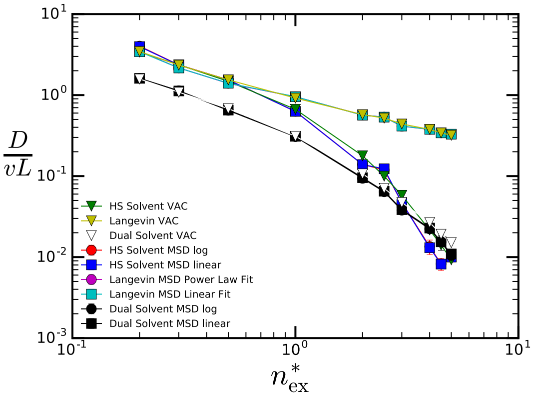

Figure 4.4: This figure shows the reduced diffusion coefficient of a 2D Lorentz gas, a pure Langevin solvent whose friction is set to the effective friction of the corresponding Lorentz gas, and a dual Langevin-Lorentz solvent with the same effective friction. The triangles refer to D extracted from the VAC, the circles have D extracted from the log-log MSD, and the squares extracted from the linear MSD fit. At low n_{ex}^{*}, which corresponds to low friction on the order of 0.1 ps^{-1}, the Langevin solvent and the hard sphere solvent have good agreement, with the dual solvent having less then half of the diffusion as each solvent in isolation. At higher n_{ex}^{*}, excluded volume effects start taking over and reducing the diffusion far below the corresponding effective Langevin friction. Notice the hints of the diffusion anomaly at higher densities, as the dual solvent overtakes the pure hard sphere solvent. This is explored in figure 4.5

excellent approximation of the LG, but as the density increases, the Langevin solvent becomes a worse approximation, due to the fact it cannot simulate excluded volume effects. It would be possible to find a γ_{T} which matched the D_{com} of a high density Lorentz gas, but the microscopic dynamics would be very different, the VACs would not match, and it would fail the requirement of dynamical consistency. Hints of the Langevin-Lorentz diffusion anomaly are present at high densities, as it appears the pure hard sphere solvent and dual solvent switch places.

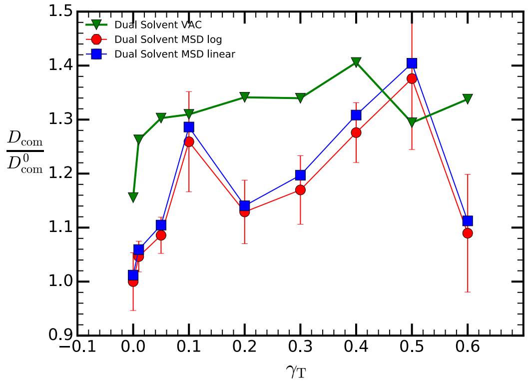

Figure 4.5: This is a plot exemplifying the diffusion anomaly in the 2D Langevin-Lorentz gas. The Lorentz solvent system has an $n^*_{\text{ex}} = 4.0$ for every point, while the Langevin friction is varied from 0 to 0.6. A Langevin friction of 0 implies a pure hard sphere, which has a diffusion coefficient of $D^0_{\text{com}} = 0.96\ \frac{2}{ps}$. As the Langevin friction is increases, the diffusion coefficient anomalously increases instead of decreasing. The red spheres are the MSD log-log fit, the blue squares are the linear MSD fit, and the green triangles are the VAC quadrature integration

A full analysis of the diffusion anomaly is shown in figure 4.5. A high density is chosen and the Langevin friction γ_{T} is varied, starting from zero. As the Langevin friction is increased, the diffusion initially increases with increasing friction. This is counter-intuitive, as the additional friction should only slow the tracer down. Figure 4.6 shows this diffusion anomaly does not extend to the rotational diffusion, which is monotonically decreasing with increasing friction.

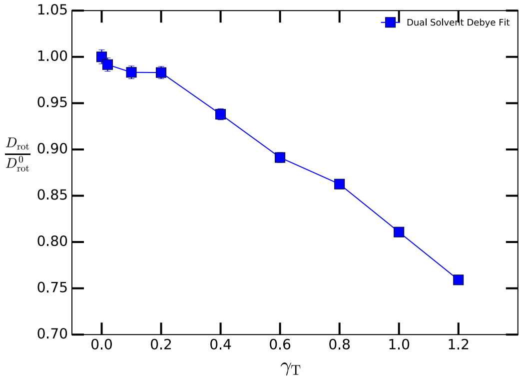

Figure 4.6: This is a plot showing the rotational diffusion coefficient under the same conditions as figure 4.5. The anomalous diffusion observed in that figure does not appear to extend to rotation, as the rotational diffusion is monotonically decreasing with additional friction.

4.5 Conclusions

We have uncovered a new unexpected anomaly in diffusion of a sphereocylindrical tracer in a Langevin solvent with hard Lorentz scatterers. This anomaly is similar to a previous anomaly discovered originally by Doi and Edwards, and expanded on by Höfling, Franosch, Tucker and Hernandez.[10,17,18] The previous anomaly was due to suppression of rotational modes as the scatterer density was increased causing additional translational diffusion. Our work shows no suppression of rotational modes, so the mechanism for our anomalous speedup must be different. We believe it is related to the time the scatterer can spend in highly confined spaces and how long it can take to rattle out at high densities. The random forces generated by a weak Langevin friction could expedite the tracer's escape of these pockets and increase the effective diffusion.

The Langevin-Lorentz solvent mixes the ability to generate excluded volume with hard scatterers with the implicit soft solvent effects of Langevin dynamics without having to evaluate a polynomial pairwise potential for every body on each time step. In addition, we have shown that the Langevin and Lorentz solvents are dynamically consistent in the low friction regime but show serious dynamical consistency issues at high excluded volume. This shows that a mixture of these solvents explores a larger area then either alone.

References

(1) R.Weilandt, D.; Hatzimanikatis, V. *Biophys. J.* **2019**, *117*, 355–368.

(2) Schnell, S.; Turner, T. *Progress in Biophysics and Molecular Biology* **2004**, *85*, 235–260.

(3) Harada, R.; Sugita, Y.; Feig, M. *J. Am. Chem. Soc.* **2012**, *134*, 4842–4849.

(4) S.Banks, D.; Fradin, C. *Biophys. J.* **2005**, *89*, 2960–2971.

(5) Regner, B. M.; Vučinić, D.; Domnisoru, C.; Bartol, T. M.; Hetzer, M. W.; Tartakovsky, D. M.; Sejnowski, T. J. *Biophys. J.* **2013**, *104*, 1652–1660.

(6) Stolle, M. D.; Fradin, C. *Biophys. J.* **2019**, *116*, 791–806.

(7) Sandev, T.; Metzler, R.; Chechkin, A. *Fractional Calculus and Applied Analysis* **2018**, *21*, 10–28.

(8) Hagy, M. C.; Hernandez, R. *J. Chem. Phys.* **2013**, *138*, 184903.

(9) Cui, Q.; Hernandez, R.; Mason, S. E.; Frauenheim, T.; Pedersen, J. A.; Geiger, F. *J. Phys. Chem. B* **2016**, *120*, 7297–7306.

(10) Tucker, A. K.; Hernandez, R. *J. Phys. Chem. B* **2010**, *114*, 9628–9634.

(11) Tucker, A. K.; Hernandez, R. *J. Phys. Chem. B* **2011**, *115*, 4412–4418.

(12) Weiss, M.; Elsner, M.; Kartberg, F.; Nilsson, T. *Biophys. J.* **2004**, *87*, 3518–2524.

(13) AlcÃązar-Cano, N.; Delgado-Buscalioni, R. *Soft Matter* **2018**, *14*, 9937–9949.

(14) Zwanzig, R. *Annu. Rev. Phys. Chem.* **1965**, *16*, 67.

(15) Hansen, J. P.; McDonald, I. R., *Theory of Simple Liquids*; Academic Press: San Diego, 1986.

(16) Gerling, R.; Hüller, A. *A. Z. Physik B - Condensed Matter* **1980**, *40*, 209–217.

(17) Doi, M.; Edwards, S. F. *J. Chem. Soc. Faraday Trans.* **1978**, *74*, 560–570.

(18) Höfling, F.; Frey, E.; Franosch, T. *Phys. Rev. Lett.* **2008**, *101*, 120605.

Chapter 5

Insight into transport anomalies in the stochastic Lorentz gas with guidance from periodic orbits

5.1 Introduction

The transport coefficients for the random Lorentz gas solvent are not analytic functions of the density, and as such are not able to be expressed in closed form. Technically, this is due to the excluded volume generating correlated collisions that cause a power series of the reduced density to diverge.[1] However, work in a relatively unknown (at least to chemists) field of physics has come up with impressive, exact equations for the diffusion coefficients for a point in an array of periodic hard scatterers, generally known as the periodic Lorentz gas. This is accomplished not by generating a series as a function of the density, but by summing over the unstable periodic orbits generated by the static background of scatterers. These orbits form a skeleton-like structure that shadows the motion of the tracer as it explores the underlying geometry.[2] Previous work have used sums of these orbits to calculate the escape rate of a point tracer leaving a trap of three hard scatterers with an astonishingly high accuracy.[3]

The accuracy of this technique is reliant on the fact that with a static background of scatterers, the periodic orbits a tracer could possibly undergo are known and calculable. In a random Lorentz gas, it is not immediately obvious how to find useful orbits, as each new instantiation of the solvent has a different structure and hence a different set of orbits. Nevertheless, we believe that periodic orbits are the key to understanding the diffusion anomalies presented previously in this dissertation, as even qualitatively they provide insight on to how these effects might be reasonably expected to occur.

In this work we focus on the basics of using periodic orbits to calculate diffusion coefficients and how this technique might be applied to a system that does not have a static background of scatterers. Looking at the system through the lens of mean field and applying techniques from statistical mechanics, we suggest paths that might lead to the quantification of diffusion anomalies in realistic systems.

5.2 Theory

5.2.1 Categorizing Orbits

The number of periodic orbits in any hard system of three or more scatterers is infinite. However, periodic orbits are a countable objects and each has unique properties. This being the case, in practice it takes quite a small number of orbits to achieve a high accuracy result. This is due to the fact that similar orbits tend to be close to each other and have similar structures, a fact called shadowing.[4] To use periodic orbits, one must first count them.

For a solvent made of hard static scatterers, it is possible to uniquely identify each scatterer with an integer. Because spheres are everywhere convex, it is impossible for a hard interaction with a sphere to cause the point tracer to hit the same scatterer twice in a row. This implies that if you have two scatterers: 1 and 2, the smallest possible periodic orbit has the tracer colliding with 1, then 2, then back to 1 *ad infinitum*. This is known as the orbit $\overline{12}$ which has length 2. Each orbit of length N has the tracer undergoing N collisions before returning to the starting point. The stability of the orbit depends on the number of collisions the tracer must undergo before returning to the starting point; as might be intuitively expected, longer orbits are more unstable.

Finally, in a confined system, there is only one type of periodic orbits,

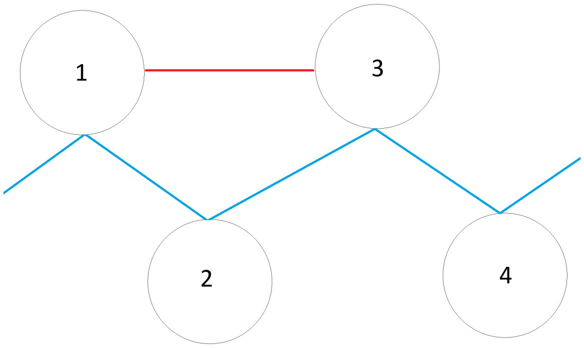

Figure 5.1: This figure demonstrates the difference between standing and traveling orbits on an infinite periodic lattice. The red line is the standing orbit $\overline{13}$. The blue line is the traveling orbit $\overline{1234}$. Orbits like the blue line contribute to the overall diffusion coefficient while red orbits detract from the diffusion.

standing orbits. Confined systems do not have long time diffusion, so for a system to exhibit transport, it must be unbounded on the time scale of observation. On an infinite periodic lattice, there are both standing orbits, ones which conclude in the same point which they started; and traveling periodic orbits, ones that end on the same point when accounting for the periodic boundary conditions, but move when looking at the lattice as a whole. See figure 5.1. These orbits are vital to the understanding of the long time diffusion of a Lorentz gas.

5.2.2 Formula and Applications

The exact equation for the translational diffusion coefficient is

$$D_{\text{com}} = \frac{1}{2d} \frac{\langle x^2 \rangle_{\text{o}}}{\langle T \rangle_{\text{o}}} \tag{5.1}$$

where d is the system dimensionality, $\langle x^2 \rangle_o$ is the average mean square displacement for all periodic orbits, and $\langle T \rangle_o$ is the average time it takes to complete one cycle of a periodic orbit.[4,5] $\langle ... \rangle_o$ is a reminder that these averages are over orbits, not time.

On first glance this equation looks strange. By definition, a periodic orbit ends in the same place it started, so how can it ever have a non-zero mean square displacement? To understand how this term can be non-trivial, remember that on an infinite periodic lattice there are orbits that are periodic in relation to the unit cell but traveling on the full lattice. These are the only orbits that contribute to $\langle x^2 \rangle_o$, and they contribute quadratically in time, as they are ballistic. All standing orbits contribute zero to $\langle x^2 \rangle_o$ but show up in the average time $\langle T \rangle_o$. This implies that all diffusion comes from the balance of standing and traveling orbits and the weight each has relative to the other.

Calculating $\langle x^2 \rangle_o$ relative to some known set of periodic orbits requires enumerating the length of each orbit relative to its stability.

$$\langle x^2 \rangle_o = \sum_p \frac{(-1)^{k+1}(n_1 + ... + n_k)^2}{|\Lambda_1 ... \Lambda_k|} \tag{5.2}$$

$$\langle T \rangle_o = \sum_p \frac{(-1)^{k+1}(\tau_1 + ... + \tau_k)}{|\Lambda_1 ... \Lambda_k|} \tag{5.3}$$

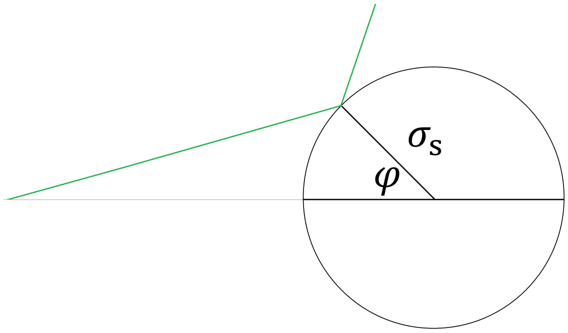

Figure 5.2: This figure shows how ϕ is defined with respect to a incident collision with a scatterer of radius σ_S. The relevant stability factor $r(\phi) = \frac{2}{\sigma_S \cos(\phi)}$. $\phi = 0$ implies to complete reversal of the tracer's velocity. The singularity at $\phi = \frac{\pi}{2}$ is due to the fact that glancing collisions are not well defined in the hard-sphere potential.

where $k = (C - 1)$ and C is the number of collisions in unique periodic orbit p. n_k is the distance traveled by the k^{th} free flight while τ_k is the time taken to travel it. Λ_k is the largest eigenvalue of the evolution matrix (called the Jacobian in the literature) for the k^{th} collision and following free flight.

For a point tracer moving through a spherical Lorentz gas, the evolution matrix for a collision and free fight is given by

$$M_k = \begin{pmatrix} 1 & \tau_k \\ 0 & 1 \end{pmatrix} \begin{pmatrix} 1 & 0 \\ r(\phi)_k & 1 \end{pmatrix} \tag{5.4}$$

where τ_k is the flight time of the k^{th} free flight and $r(\phi)_k = \frac{2}{\sigma_s \cos(\phi_k)}$ where σ_s is the scatterer radius and ϕ is the internal angle from the horizontal the scatterer makes with the tracer at the point of collision, see figure 5.2. Letting $\lambda_{k1}, ..., \lambda_{kn}$ be the eigenvalues of M_k arranged form largest to smallest, $\Lambda_k = \lambda_{k1}$.

To apply equation 5.1 to a low density random Lorentz gas in 2D, we assume a statistically periodic box with one particle in the center and a tracer moving at an average speed $\langle v \rangle$.

We then look at a one-orbit calculation for this system. We assume one traveling orbit designated $p = 1$, which has two bounces ($k = 1$). These collisions take place at approximately a $\frac{\pi}{4}$ angle from the normal. The distance of the orbit is equal to one mean free path l and the period of the orbit is $\frac{l}{\langle v \rangle}$. For a low density point tracer in the Lorentz gas, $l = \frac{1}{\rho \sigma_s}$, where ρ is the density and σ_s is the scatterer radius. Equation 5.1 then becomes (Λ cancels)

$$D = \frac{1}{4} \frac{l^2}{l \langle v \rangle^{-1}} \tag{5.5}$$

$$D = \frac{1}{4} l \langle v \rangle \tag{5.6}$$

$$D = \frac{1}{4} \frac{\langle v \rangle}{\rho \sigma_s} \tag{5.7}$$

which is comparable to the low density limit from kinetic theory, $D = \frac{3}{16} \frac{\langle v \rangle}{\rho}$.[6]

To improve this calculation, we consider one standing orbit $p = 2$, in addition to the traveling orbit shown above. This standing orbit is also of length two and has two bounces between two scatterers. $\langle x^2 \rangle$ is the same as before, as standing orbits do not contribute to the MSD. However,

$$\langle T \rangle = \frac{\tau_1}{|\Lambda_1|} + \frac{\tau_2}{|\Lambda_2|} \tag{5.8}$$

and so

$$D = \frac{1}{2d} \frac{\frac{(n_1)^2}{|\Lambda_1|}}{\frac{\tau_1}{|\Lambda_1|} + \frac{\tau_2}{|\Lambda_2|}} \tag{5.9}$$

assuming $\tau_1 = \tau_2 = \frac{l}{\langle v \rangle}$ and $n_1 = l$.

$$D = \frac{1}{2d} \frac{l^2}{\frac{l}{\langle v \rangle}\left(1 + \frac{|\Lambda_1|}{|\Lambda_2|}\right)} \tag{5.10}$$

if $l \gg \sigma_s$, which is true at low density, $\frac{|\Lambda_1|}{|\Lambda_2|} = 2$ and

$$D = \frac{1}{6} \frac{\langle v \rangle}{\rho \sigma_s} \tag{5.11}$$

which is within 15% of the value from kinetic theory.

5.3 Discussion and Conclusion

The previous section showed that simple assumptions and a small number of orbits can get answers of reasonable accuracy. The insights from equation 5.1 are more general then the quantitative results might suggest, as thinking in terms of traveling and standing orbit stability helps make sense of the diffusion anomalies that have been observed so far. For instance, in the high density Lorentz gas, the tracer spends a long amount of time rattling in confined spaces. The orbits associated with these spaces are mostly standing orbits, not contributing to the diffusion. Adding a Langevin solvent has two effects. First, it reduces $\langle v \rangle$, which universally slows the diffusion; second, it reduces the stability of all orbits via random kicks. If traveling and standing orbits were on equal footing, this effect would be a wash, but at high density the number of standing orbits outnumber the number of traveling orbits significantly, so destabilizing all orbits can increase the diffusion as long as the effect of reduced stability can overcome the reduction in average velocity.

Understanding how the stability of orbits change along a trajectory is also important. Consider the original diffusion anomaly mentioned in chapter 2 for a thin needle in two dimensions. At high density, the needle rattles in an effective tube of scatterers. The periodic orbits associated with this rattling are standing orbits, and as shown in equation 5.4 the stability of an orbit decreases with every collision along the orbit. Higher densities increases the rattling frequency and cause more rattling collisions per unit time, destabilizing these standing orbits. Traveling orbits with slow rotation are not affected by this analysis, so these orbits contribute more to the diffusion as density increases, at least until the glassy regime.

In conclusion, complex dynamics depend both on the dynamical equations of motion, and the underlying geometrical structure of of the system. This geometrical structure can, in certain cases, cause unusual and counter-intuitive effects on the overall system dynamics. Mathematically analyzing the periodic orbits generated by the geometrical structure of the system is a useful technique to understanding how this geometrical structure may effect long time dynamics.

References

(1) Bruin, C. *Physica* **1974**, *72*, 261–286.

(2) Cvitanović, P. *Physica D* **1991**, *51*, 138–151.

(3) Cvitanović, P.; Eckhardt, B. *Phys. Rev. Lett.* **1989**, *63*, 823.

(4) Cvitanović, P.; Artuso, R.; Mainieri, R.; Tanner, G.; Vattay, G., *Chaos: Classical and Quantum*; Niels Bohr Institute: Copenhagen, 2016.

(5) Cvitanović, P. *Physica D* **1995**, *83*, 109–123.

(6) Moreno, A. J.; Kob, W. *Europhys. Lett.* **2004**, *67*, 820–826.

Chapter 6

Solvent softness effects on unimolecular chemical reaction rate constants

6.1 Introduction

The prediction of global thermodynamic properties from microscopic parameters is of fundamental importance to chemistry. Dynamic systems, including transport and rates of reaction behave non-linearly with variation of microscopic parameters. Extracting these parameters *Ab inito* can be both difficult analytically and expensive computationally. In order to make real systems tractable, coarse graining (CG) is often valuable. The theory behind coarse graining is well developed.[1,2] Ultra Coarse Graining has been successfully use in interfacial systems.[3] However, CG can change the dynamics of a system in unphysical ways.[4] Mapping the dynamics of CG systems to real system can also be an issue.[5]

We recently introduced the requirement for dynamical consistency[6,7] on multi-scale equations of motion to correctly reflect the timescales at each level of representation. This is a challenge to most bottom-up coarse-graining procedures because the potentials of mean force resulting from partial integration of partition functions are not, by said construction, the potential of a Hamilton-Jacoi equation of motion. Projection operator techniques include the potential of mean force (PMF) and can lead to correct time scales if all the projective terms are included carefully,[8] as was done to second order in our earlier work[6] on Janus particles. Here, we follow a complimentary coarse-grained approach in which we use a top-down representation of a simplified solvent to model the solvent response function. We use it to confirm that the reaction dynamics of the solutes in this solvent are dynamically consistent.

Rates of reaction have been studied since the beginning of chemistry. Pioneered by Eyring and Wigner, a major theoretical model for obtaining the standard rate of reaction approximately —if sometimes exact— is transition state theory.[9–11] It plays a major role in characterizing the solvent effects in the context of Kramers' turnover theory.[12,13] Obtaining such reaction reacts exactly and directly can be computationally very expensive. Reaction pathways can be complicated for many reasons including the complexity arising from multi-dimensional, non-linear and many-body solvent interactions. The use of CG in simplifying reaction rate simulations has been previously attempted,[14] although much cheaper than first principles models, current CG models are still expensive and can suffer from dynamical inconsistency between scales.

Our group recently introduced an efficient coarse graining technique: the stochastic hard collision (SHC) potential.[15],[16] Attempts to combine soft and hard dynamics have been pursued before by several groups, and includes the use of stochastic momentum swapping between disparate particles.[17] The SHC solvent allows a degree of solvent softness while maintaining the efficient computational speed of a hard sphere solvent. In one-dimension, an SHC rod can represent a complex, soft entity such as polymer that, in addition to direct collisions, has a chance to slip past other rods. The SHC solvent has several intriguing properties regarding the effects on they dynamics of solutes which have already been reported.[18] It remained to demonstrate the SHC solvent can be used to properly model the rate of a solvated unimolecular reaction. In so doing, this work reveals the effect of solvent softness on unimolecular reaction rates of a hard tracer in a sea of SHC particles.

6.2 Theory

6.2.1 The Stochastic Hard Collision (SHC) Solvent

The solvent particles in our simulation undergo stochastic hard collisions parameterized by the stochastic softness parameter δ. Solvent particles separated by a distance $r > \sigma$ have no interaction and their potential is zero. When two solvent particles, labeled i and j, come in contact —that is, when $r_{ij} = \sigma$— at some time t_{col}, a random number $0 \leq a_{ij} \leq 1$ is generated to determine the nature of the collision. If $a_{ij} \geq \delta$, the interaction is taken to be a hard collision in the usual sense. If $a_{ij} < \delta$, particles i and j enter a bimolecular 'ghosting' state in which the particles avoid a collision because the potential between them is zero. It remains zero independent of distance until such time as the particles are separated by a distance greater than σ.

Since the ghosting state lasts until the interparticle distance once again exceeds σ, and the particles continue to move towards each other immediately after the avoided collision, the ghosting state can continue for a seemingly arbitrary amount of time. The interaction potential can be summarized as:

$$V_{ij}^{\mathrm{SHC}}(r) = \begin{cases} 0, & r > \sigma \\ 0, & r \leq \sigma \text{ and } a_{ij}\left(t_{\mathrm{col}}\right) < \delta \\ \infty, & r \leq \sigma \text{ and } a_{ij}\left(t_{\mathrm{col}}\right) > \delta \end{cases} \tag{6.1}$$

where it is implied that each pair of particles has a history that affects the state and the corresponding last collision time. The ghosting state between a given pair of particles (i, j) has no relation to their interaction with particle k because all interactions are independent and pairwise. Any particle can be ghosting with any number of particles at the same time.

6.2.2 Kramers' Turnover Theory

The rate constant of a reaction across a barrier in the modern version of Kramers' reaction rate theory can be written as a product of three principal terms as[13,19]

$$k_{\mathrm{K}} = \Gamma_{\mathrm{TST}}\kappa_{\mathrm{PGH}}\Upsilon_{\mathrm{s}} \tag{6.2}$$

where Γ_{TST} is the standard transition state theory rate, κ_{PGH} is the spatial diffusion factor (also called the Pollak-Grote-Hynes transmission factor), and Υ_{s} is the depopulation factor.[20] The standard transition state rate in Kramers' theory for the escape across the barrier of a quartic potential is given by[12]

$$\Gamma_{\mathrm{TST}} = \frac{\omega_r}{2\pi} e^{-\beta E_b} \tag{6.3}$$

where ω_r is the characteristic well frequency obtained from the harmonic approximation to the bottom of the double well, and E_b is the height of the energy barrier. The spatial diffusion factor is often given as a function of the friction γ, assuming the friction is constant and uncorrelated. The spatial diffusion factor can be expressed in the form,[21]

$$\kappa_{\mathrm{PGH}} = \frac{1}{\omega_{\mathrm{b}}} \left(-\frac{\gamma}{2} \sqrt{\frac{\gamma^2}{4} + \omega_{\mathrm{b}}^2} \right) \tag{6.4}$$

where ω_{b} is the harmonic frequency at the top of the barrier.

The depopulation factor is an extension of the transmission factor —viz, a correction to the transition state theory rate— to include the exchange of energy between the reactive particle and the effective friction of the solvent bath. In order to compute it, one needs to find the average energy lost to the bath while the RP travels across the barrier region: $\beta\langle \Delta E \rangle$.[13,19] To calculate this average loss, we integrate the phase space volume below the barrier top to obtain

$$\beta\langle \Delta E \rangle = \frac{2}{3} \frac{\gamma r_{\mathrm{c}} \sqrt{M\epsilon}}{k_{\mathrm{B}} T} \tag{6.5}$$

where M is the tracer mass, ϵ is the energy difference between the well bottom and the barrier top, and r_c is the distance between the well bottom and well top. The full expression for the depopulation factor for a single well system is then given by

$$\Upsilon_s(\kappa) = e^{\left(\frac{2}{\pi}\int dt \frac{\ln\left(1-\mathrm{Exp}\left[-\kappa\frac{t^2+1}{4}\right]\right)}{t^2+1}\right)}. \tag{6.6}$$

In order to compute $\Upsilon_s(\kappa)$, we numerically evaluate the integral in Eq. 6.6 from 0.0001 ps to 400 ps, avoiding the singularity at 0 and integrating long enough to converge it.

6.3 Numerical Methods

6.3.1 Reactive Particle and Solvent Bath

The reactive particle (RP) lives on a 1D double-well potential given by

$$V^{\mathrm{RP}}(x) = \epsilon\left(\frac{1}{r_c^4}x^4 - \frac{2}{r_c^2}x^2 + 1\right) \tag{6.7}$$

where x is the RP's position on the line, ϵ is the barrier height and r_c is the characteristic distance between the well bottom and the top of the barrier. The parameters are set at a typical diatomic molecular bond distance with $r_c = 3$, near room temperature of 300 K, and a barrier height that is higher than the temperature by varying ϵ between 2 and 5 $k_\mathrm{B}T$. The RP has a hard sphere diameter of 3 and always undergoes a hard collision with any solvent particle that moves within its collision radius. Unlike the solvent-solvent interaction, the RP never ′ghosts′ with solvent particles.

The RP lives in a solvent bath of 300 solvent particles which we found was large enough to avoid finite size effects. The solvent particles move ballistically along the line and collide with other solvent particles under the stochastic hard collision (SHC) potential in Eq. 6.1 parameterized by δ. The solvent particles have a collision diameter of 3 with both other solvent particles and the RP. This choice makes the diameters for all particles to be equal, and the same as the distance between the minima of the RP. Deviations from these equalities would tend to favor some motions over others, and hence would present simpler limiting cases to the one considered here.

The system is initialized at $t = 0$ with the reactive and solvent particles placed equidistantly from each other with a random velocity obtained from a Maxwell-Boltzmann distribution at the system temperature, T. The RP is initially restricted to the reactant well by placing it in a harmonic potential with a minimum position and frequency matching that of the reactant side of the double well. The system is then equilibrated for 50,000 global collisions.

Once the equilibration is complete, the harmonic potential is replaced instantly by the double well potential in what is as close as possible to a constant energy transition. If upon this potential switch, the total kinetic energy of the RP is greater than the change in potential energy, then an equiergic transition is possible and the kinetic energy is rescaled to cover the change in potential. If instead, the total kinetic energy is less then the change in potential, then an equiergic transition is not possible because the kinetic energy would have to be negative to fully cover the gap between the potentials. In this case, the kinetic energy is set to zero to make the gap as small as possible.

6.3.2 Reaction and Rate Constant Calculation

Once the system has equilibrated at an initial distribution constrained to the reactant side for a RP on the double-well potential, then an ensemble can be propagated to determine various dynamical properties. The time of a given transition is recorded as follows: The RP moves until it comes within 1 $k_B T$ of one of the two well bottoms. Once this happens, the RP is 'tagged' to that well, and the timer on the first passage time is started. The RP is then free to move under the influence of the potential and solvent particles until it crosses the barrier top, at which point the unimolecular reaction is said to have occurred, and the timer is stopped at the first passage time for that trajectory.

Thereafter, the reactive particle and solvent background are regenerated and re-equilibrated and the process is repeated to obtain another first passage time. A series of these first passage times Δt are stored for each trajectory.

We use two complementary methods to extract the reaction rate constant from the values of Δt obtained from the trajectories. First, we average the Δts to find the mean first passage time (MFPT), τ_{MFPT}. This τ_{MFPT} across the barrier is inversely proportional to the reaction rate,

$$k_{\text{MFPT}} = \frac{1}{\tau_{\text{MFPT}}} \tag{6.8}$$

which is known to be exact in the special case of a harmonic barrier.[13] Second, we obtain a rate by numerically examining the rate of population decay. Specifically, we order the values of Δt in a list from smallest to largest. The fraction $P(t)$ of the population that remains after a given time t is the fraction of these trajectories that have a $\Delta t \geq t$. As we generate this fraction numerically, we record it at discrete time steps, $t = n\Delta t'$ for an integer n and $\Delta t'$ equal to 1.0 ps. We then fit these points to an exponential decay,

$$P_{\text{Traj}}(t) = e^{-\alpha t_{\text{F}}} \; . \tag{6.9}$$

The resulting fitting parameter, α, is the rate, k_{TD}.

6.3.3 Numerical Analysis

Our theoretical calculations require a number of variables that cannot be computed *a priori*, and must be extracted from simulation. In particular, the effective friction the reactive particle experiences is a consequence of the random collisions with the solvent. In order to extract this friction, we calculate the velocity autocorrelation function (VAC) of the reactive particle using Eq. 6.10 and fit it to Eq. 6.11.

In order to extract the friction responding to a quasi-bound RP, we use a harmonic potential to propagate it with the same spring constant as the bottom of the double well potential as we do to equilibrate the initial distribution on the reactant side. We then collect velocity data for the RP every 100 time steps.

$$\mathrm{VAC}(\Delta t) = \frac{\langle \vec{v}(t) \cdot \vec{v}(t + \Delta t) \rangle}{\langle \vec{v}(t)^2 \rangle} \tag{6.10}$$

$$F_{\mathrm{VAC}}(t) = \cos(\omega t + \phi) e^{-\gamma t} \tag{6.11}$$

where γ is the friction coefficient. A characteristic VAC is shown in Fig. 6.1. The friction can also be approximated using the force autocorrelation function (FAC). In an instantaneous hard collision, the force is not well defined; however, the impulse is. In order to calculate the FAC, we assume the impulse

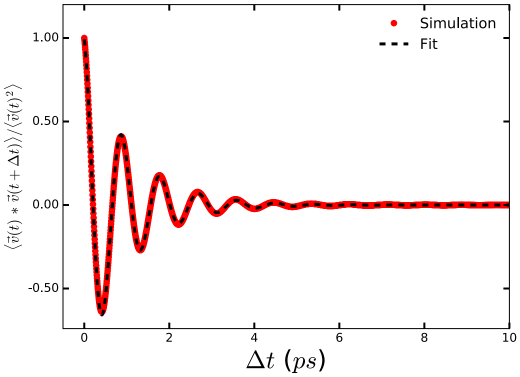

Figure 6.1: A typical velocity autocorrelation function (solid red curve) for the reactive particle in a harmonic potential solvated by 300 SHC particles compared to the least-squares fit (dashed black curve) of the cosine exponential form in Eq. 6.11. This particular system correspond to $T = 300\,\text{K}$, $\delta = 0.25$, and $\epsilon = 2kT$, for which $\omega = 6.951\ \text{ps}^{-1}$,$\phi = 0.1316$, $\gamma = 0.9892\ \text{ps}^{-1}$ with an $R^2 = 0.999159$.

of the collision is spread evenly across a single simulation time step (t_{step}) of 0.005 ps. In addition, we ignore forces resulting from the double well potential, as only solvent collisions contribute to the friction. The FAC can then be calculated using Eq. 6.10 with the velocity $\vec{v}$ replaced with the force $\vec{F}$. It is approximated by a delta function resulting from the uncorrelated nature of the solvent collision forces. Under this assumption, the friction can be calculated directly from the value of $\vec{F}(0)^2$ according to the relation,

$$\gamma = \frac{\vec{F}(0)^2 t_{\text{step}}}{2k_{\text{B}}TM}\,. \tag{6.12}$$

In order to extract the harmonic frequency of the well and barrier, we must find the potential of mean force (PMF) that the reactive particle experiences.

The PMF is generated by running Monte Carlo (MC) simulations of the 300 tracer and one reactive particles in identical conditions to the MD simulations. In each step of the MC simulation, all particles are assigned a possible new location within its designated move zone. The full box width of 1806 spans the designated move zone for the solvent particles. The RP is restricted to a smaller designated move zone of 4.5 from the barrier top in either direction. Once the possible location is chosen, a random number α between 0 and 1 is generated. For solvent particles, the move is rejected if there is a RP overlap or if α is greater then δ^N where N is the number of solvent overlaps, and rejected otherwise. For the reactive particle, the move is accepted if there are no solvent overlaps and $\alpha < e^{\frac{-\Delta E}{k_\mathrm{B} T}}$ where ΔE is the potential energy difference between the current location and the new location.

After all particles have experienced an attempted move, the locations of every particle is recorded. This process is repeated 500 million times and the locations of the RP are placed into a normalized histogram to generate a probability distribution. The PMF is related to the probability distribution via $V_\mathrm{PMF}(x) = -kT\ln(P(x))$ which can be represented as

$$V_\mathrm{PMF}(x) = a(x-W)^4 + b(x-W)^3 + c(x-W)^2 + d(x-W) + e \qquad (6.13)$$

Once the PMF is found, we fit the well and barrier to two independent quartic

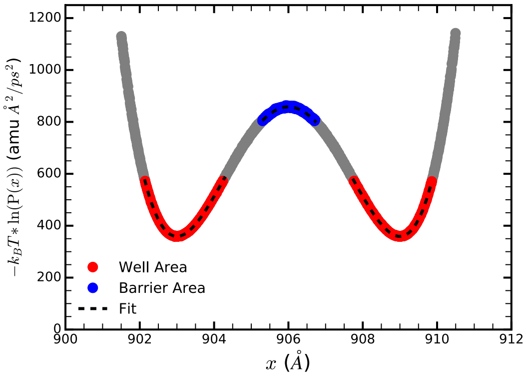

Figure 6.2: A characteristic PMF obtained by Monte Carlo (MC) sampling for a reactive particle in the SHC solvent under the same conditions as Fig. 6.1. The wells were fit to a quartic potential (using only the red points ovelapping the dashed line) resulting in values of $a = 6.157$, $b = -23.132$, $c = -78.255$, $d = 187.79$ $e = 764.87$, $W = 905.06$ with residual equal to $R^2 = 0.999813$ Similarly, the barrier was fit to a quartic potential (using only the blue points ovelapping the dashed line) resulting in values of $a = 14.692$, $b = -71.611$, $c = 15.979$, $d = 175.277$ $e = 717.816$, $W = 904.774$ with residual equal to $R^2 = 0.975657$

equations, given by Eq. 6.13, and use these to find the approximate harmonic coefficient at the point of inflection. A characteristic PMF and these fits are shown in Fig. 6.2. Each harmonic potential is fitted independently, and is only expected to be accurate in the region near the well bottom or barrier top. Once the harmonic terms are fitted, they are used, along with the friction and effective barrier height to compute the theoretical unimolecular rate for barrier crossing. (See Sec. 6.2.2.)

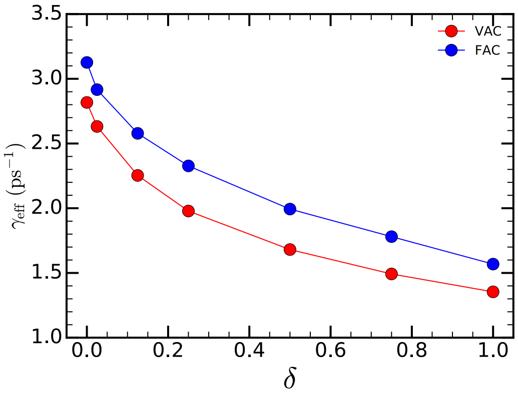

Figure 6.3: The friction extracted from the VAC (red points) and FAC (blue points) fits. The potential the RP experiences is a harmonic with the same spring constant as the RP would feel at the bottom of the well in the double well potential with $\epsilon = 2$ $k_{\text{B}}T$. All of these simulations are done with 1 RP and 300 solvent particles.

6.4 Results and Discussion

The friction as a function of δ can be extracted from the correlation function shown in Fig. 6.3. This friction is gathered from a tracer in a harmonic potential with a spring constant equivalent to the harmonic approximation at the bottom of the double well with $\epsilon = 2\ k_{\text{B}}T$. We repeated this calculation for each ϵ studied here, but there were no significant differences between them. This is expected, as the effective friction is generated by the chaotic motions of the solvent particles, not the harmonic potential.

Figure 6.4 compares the results of variables used in the theoretical calculation of the rate constant (see Sec. 6.2.2) with those same variables extracted from a PMF generated from MC simulations. There is not a large difference between the variables generated from MC compared to the bare potential, meaning that the main changes in the rate constant come from the change in effective friction, not from changes in the effective PMF.

The rates extracted from MD, as well as the theoretical rates calculated using Kramers' theory and MC results are shown in Fig. 6.6. A single $k_{\mathrm{B}}T$ is shown in Fig. 6.5. The unimolecular rate constant appears to match Kramers' theory well, which implies that the rates experienced by a RP in the SHC solvent are not so different from a more complex soft solvent system. The rate decreases monotonically with δ, as expected given that a softer solvent should mean a lower rate in the under damped regime.

As shown in Eq. 6.2, the theoretical rate constant is broken down into three main terms. The first term, the TST rate, has units while the other two are unit-less correction factors between 0 and 1. How these other two factors change with the effective friction is well understood, there are two regimes: the under damped regime and the over damped regime.

In the under damped regime, the rate constant is energy diffusion limited. That is, the bottleneck of the reaction is the accumulation of enough energy for the particle to be above the barrier. Above this threshold, a RP moves quickly toward (and past) the barrier without being slowed down by the weak friction. The process to get above the threshold is slow because the weak coupling also

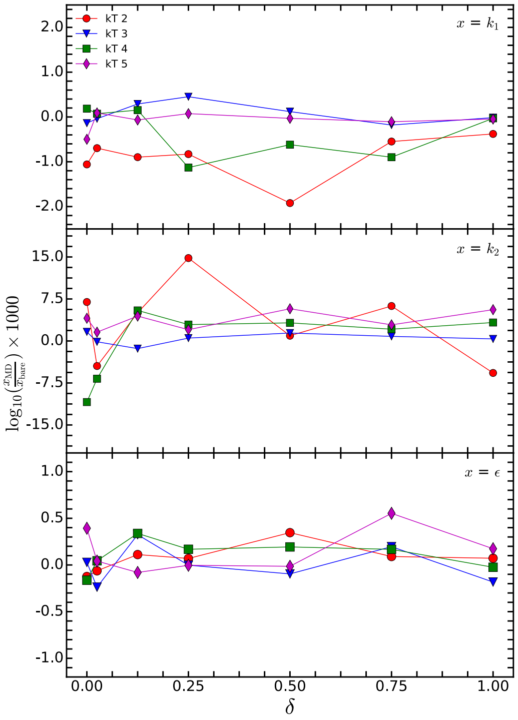

Figure 6.4: A triple plot showing how the relevant factors change between the bare potential given in eqn. 6.7 and the MC simulations. The top plot references the effective spring constant at the bottom of the well, k_1, the middle plot references the spring constant at the top of the barrier, k_2, and the bottom plot references the distance between the top of the barrier and the bottom of the well, ϵ. Each color represents a different ϵ, with red representing $\epsilon = 2k_{\rm B}T$ and so on.

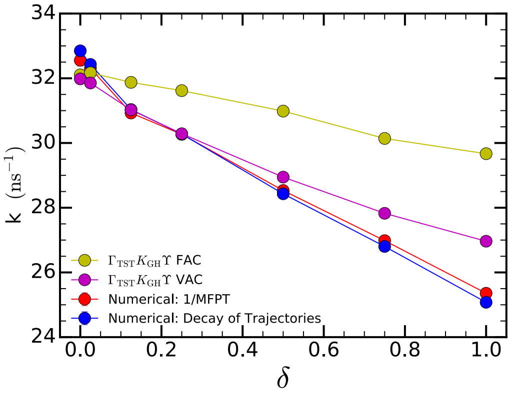

Figure 6.5: The unimolecular rate constant for barrier crossing, K, as a function of δ for $\epsilon = 3k_{\mathrm{B}}T$. All simulations have 1 RP and 300 solvent particles.

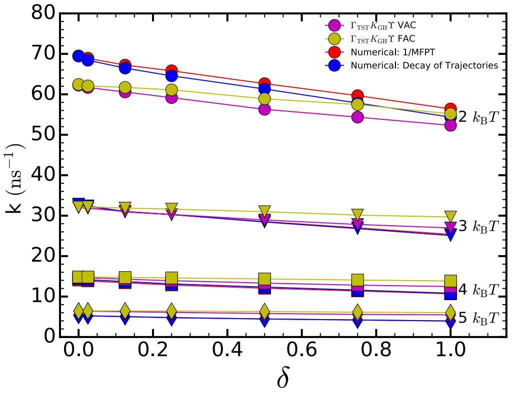

Figure 6.6: The unimolecular rate constant for barrier crossing, K, as a function of δ. The red and blue points are MD numerical results. The yellow and magenta points are the theoretical results using Kramers' rate theory. They differ by the method used to compute the friction. The points that use the friction as extracted from the VAC are magenta and the yellow use the FAC to extract the friction. The labels on the right denote the value of ϵ in units of $k_{\mathrm{B}}T$. All simulations have 1 RP and 300 solvent particles.

exerts very weak energy exchanges, requiring a statistically large number of kicks to build the necessary accumulation. In this regime, the depopulation factor is relevant because it accounts for the probability of building up the requisite energy accumulation, and the spatial diffusion factor is very close to 1.

Likewise, in the over damped regime, the rate constant is limited by position, as the large friction means larger kicks so the bottleneck is getting near the barrier, not getting enough energy to get over it. In this regime, the spatial diffusion factor is relevant, and the depopulation factor is close to 1.

We break down the factors that go into the rate constant and separate the two major coefficients to the standard rate in Fig. 6.7. This shows the system goes through a Kramers' turnover: the system moves from an over damped regime near the critical regime, to an under damped regime.[22] The transition happens very close to $\delta = 0$ so it is not visible as a peak in the rate in Fig. 6.5. The monotonic decrease in the rate constant, is due to decreasing friction in the under damped regime. An increase in the SHC solvent scatterer density should increase the effective friction the RP feels at every delta, and make the turnover clearer.

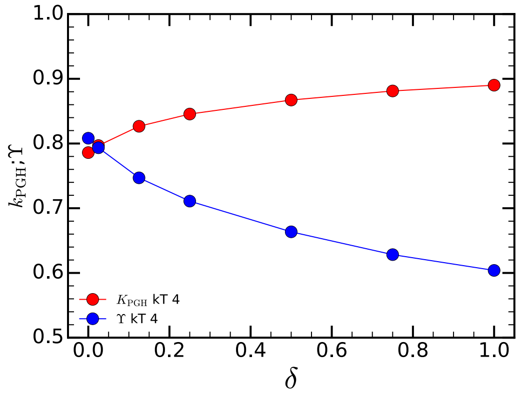

Figure 6.7: Theoretical factors constirbuting to Kramers' rate, $\kappa_{\rm PGH}$ and Υ, vs. δ. $\kappa_{\rm PGH}$ and Υ are numbers between 0 and 1. In the under damped regime of low γ, Υ dominates the rate and $\kappa_{\rm PGH}$ is close to 1. In the over damped regime of high γ the reverse happens. These results are from $\epsilon = 3k_{\rm B}T$, but is representative of all ϵ values studied here.

6.5 Conclusions

In this work, we have shown the SHC solvent system, when coupled to a reactive particle (represented by a double well potential) can elicit dynamics in that particle that are statistically similar to that from an all-particle or all-atom solvent. In particular, the rate constants observed in the reaction of the particle coupled to the SHC solvent match those of the Kramers' transition state theory rates for a particle escaping a well in the corresponding Langevin bath. This suggests that the SHC solvent system can act as a tunable solvent that can be used to extract rates of more complex reactions without requiring the expense of more fine-grained representations of the solvent.

Tunable coarse grained solvents have been highly sought after, as the ability to model complex environments properly allows for a multitude of computational experiments to be carried out. Many have looked at implicit solvents for general molecular dynamics,[23] but there are also examples of coarse grained explicit solvents such as the MARTINI force field.[24] The SHC solvent is useful because it generates excluded volume like an explicit solvent but also induces a wide range of effective frictions similar to an implicit solvent.

Changing the softness of the solvent can effect the resultant rate of reaction and can move the system through a Kramers' turnover regime. Although Kramers initially suggested such a turnover must exist, it was not until recently that such as transition was directly observed in computational[**hern08g**] and experimental[25] systems. Observing this regime change implies that the changes in friction caused by changes in solvent softness are significant compared with the internal scale of the system. Changing the SHC solvent softness can meaningfully change the effective frictions the system experiences for low computational cost.

The SHC solvent allows for hard interactions to generate long range correlations that can be difficult for implicit solvent systems, such as the Langevin solvent, to represent while also not having unrealistically impermeable excluded volume effects of a pure hard sphere system. It also does not require integrating a polynomial bimolecular potential term on every time step for each solvent particle. A challenge to the use of the SHC solvent is that it is discrete rather than smooth and hence does not readily interface with typical Molecular Dynamics integrators that rely on smooth and deterministic potentials.

It would be interesting to see how the SHC solvent performs in a more realistic rate system, for instance with an isomerization reaction in 3 dimensions. Some work would have to be done combining the hard SHC interactions with soft intermolecular interactions of an organic molecule, but once the details were worked out it would be a test case for the practicality of using the SHC solvent on a larger scale. Previous work has looked at the expansion of the SHC solvent to a hard-core soft-shell model and how this extension impacts the effective packing fraction and thermodynamic behavior.[26] This model would not be very effective for a 1 dimensional rate system because solvent particles would be unable to reorder themselves. If the system was extended to 2 or 3 dimensions, however, it would be a more realistic expression of the SHC solvent at no additional computational cost.

References

(1) Dama, J. F.; Sinitskiy, A. V.; McCullagh, M.; Weare, J.; Roux, B.; Dinner, A. R.; Voth, G. A. *J. Chem. Theory Comput.* **2013**, *9*, 2466–2480.

(2) Davtyan, A.; Dama, J. F.; Sinitskiy, A. V.; Voth, G. A. *J. Chem. Theory Comput.* **2014**, *10*, 5265–5275.

(3) Jin, J.; Voth, G. A. *J. Chem. Theory Comput.* **2018**, *14*, 2180–2197.

(4) Depa, P.; Maranas, J. *J. Chem. Phys.* **2005**, *123*, 094901.

(5) Wagnera, J. W.; Damaa, J. F.; Durumeric, A. E. P.; Voth, G. A. *J. Chem. Phys.* **2016**, *145*, 044108.

(6) Hagy, M. C.; Hernandez, R. *J. Chem. Phys.* **2013**, *138*, 184903.

(7) Cui, Q.; Hernandez, R.; Mason, S. E.; Frauenheim, T.; Pedersen, J. A.; Geiger, F. *J. Phys. Chem. B* **2016**, *120*, 7297–7306.

(8) Pivkin, I. V.; Karniadakis, G. E. *Phys. Rev. Lett.* **2008**, *101*, 118105.

(9) Eyring, H. *J. Chem. Phys.* **1935**, *3*, 107–115.

(10) Wigner, E. P. *J. Chem. Phys.* **1937**, *5*, 720–725.

(11) Truhlar, D. G.; Garrett, B. C.; Klippenstein, S. J. *J. Chem. Phys.* **1996**, *100*, 12771–12800.

(12) Kramers, H. A. *Physica (Utrecht)* **1940**, *7*, 284–304.

(13) Hänggi, P.; Talkner, P.; Borkovec, M. *Rev. Mod. Phys.* **1990**, *62*, 251–341.

(14) Ridgway, D.; Broderick, G.; Lopez-Campistrous, A.; RuâĂŹaini, M.; Winter, P.; Hamilton, M.; Boulanger, P.; Kovalenko, A.; J.Ellison, M. *Biophys. J.* **2008**, *94*, 3748–3759.

(15) Craven, G. T.; Popov, A. V.; Hernandez, R. *J. Chem. Phys.* **2013**, *138*, 244901.

(16) Craven, G. T.; Popov, A. V.; Hernandez, R. *Soft Matter* **2014**, *10*, 5350–5361.

(17) Donev, A.; Alder, B. J.; Garcia, A. L. *Phys. Rev. Lett.* **2008**, *101*, 075902.

(18) Craven, G. T.; Popov, A. V.; Hernandez, R. *J. Chem. Phys.* **2015**, *142*, 154906.

(19) Ianconescu, R.; Pollak, E. *J. Phys. Chem. A* **2016**, *120*, 3155–3164.

(20) Mel'nikov, V. I.; Meshkov, S. V. *J. Chem. Phys.* **1986**, *85*, 1018–1027.

(21) Pollak, E.; Grabert, H.; Hänggi, P. *J. Chem. Phys.* **1989**, *91*, 4073–4087.

(22) Tiwarya, P.; Berne, B. J. *J. Chem. Phys.* **2016**, *144*, 134103.

(23) Kleinjung, J.; Fraternali, F. *Curr. Opin. Struct. Biol.* **2014**, *25*, 126–134.

(24) Marrink, S. J.; Risselada, H. J.; Yefimov, S.; Tieleman, D. P.; de Vries, A. H. *J. Phys. Chem. B* **2007**, *111*, 7812–7824.

(25) Rondin, L.; Gieseler, J.; Ricci, F.; Quidant, R.; Dellago, C.; Novotny, L. *Nature Nanotechnology* **2017**, *12*, 1130–1133.

(26) Singh, R. S.; Hernandez, R. *Chem. Phys. Lett.* **2018**, *708*, 233–240.

Chapter 7

Conclusion and Future Work

7.1 Concluding Remarks

This work has explored the effect of structure on the dynamics of simple solvated systems. We have looked at how the order parameter for transport coefficients change with respect to dimensionality. We have examined how the addition of a soft implicit solvent affects the dynamics when combined with a hard excluded volume generating solvent, and in the process discovered a new diffusion anomaly. Searching for new insights into this anomaly has led us to finding multidisciplinary solutions that apply to previous work as well as our own. Finally, we searched for a way to tune the effects of hard solvents without having to do expensive bimolecular potential calculations. Overall, a theme of this work is that paying attention to the underlying structure of the system is key to understanding its dynamics. Dynamics do not just happen in the equations of motion, but as the final result of all the part of the system interacting. The fact that dynamics are complicated is the reason we can exist at all, for if the universe were so simple we could fully understand it, we would be so simple that we wouldn't.

7.2 Future Work

The projects mentioned in this work have many unexplored directions that our group could pursue. It would be interesting to know if the Langevin-Lorentz diffusion anomaly extends to a three dimensional system or, if like the previously discovered enhanced diffusion regime, it vanishes when the system becomes three dimensional. In addition, the precise reason the enhanced diffusion regime disappears in three dimensions was never completely understood. It is possible that the enhanced diffusion regime would re-appear if the tracer or scatterers were extended into platelets or more complex geometric structures. Aside from changing the structure of the tracer or scatterers, more distributions of scatterers could be explored. Currently, random and periodic distributions have taken the spotlight, but a self-correlated distribution could explore how density fluctuations may lead to anomalous diffusion.

The stochastic hard collision solvent holds promise, and our group has already begun exploring how extensions of this solvent can be used.[1] More work is still to be done; and in particular it would be interesting to find systems that could easily switch to a hard solvent for a large computational speedup. A self-correlated SHC solvent could also be explored, where the softness parameter extended beyond the bimolecular and included how many particles were currently overlapping with the particular solvent particle. This could make it easier for small numbers of particles to overlap while maintaining the excluded volume effect for larger numbers of particles, creating a more realistic system.

Finally, we believe that periodic orbit theory is understudied in the practical fields of chemical dynamics. The theory is mostly confined to physics, but the potential to apply it to more realistic and impactful systems exists. The fundamental structure of the theory is sound and, although finding the right approximations and limiting cases to apply it to chemical systems would be difficult, the rewards would surely be worth it. It could both provide a new lens for understanding chemical systems and become the most accurate and powerful mathematical machinery for insight into the fundamental link between microscopic systems and macroscopic phenomenon since the discovery of statistical mechanics.

References

(1) Singh, R. S.; Hernandez, R. **2018**, *708*, 233–240.

Appendix

This appendix includes figures presenting data that support the narrative in the main text, and which may be useful to the reader in replicating the data. These figures were generated from the 2D and 3D spherocylinder Lorentz gas, Langevin solvent, and SHC system. Many plots refer to tests that ensure the models studied here respect the appropriate limits and do not have any unexpected finite size effects. Figures A.1 - A.7 refer to the two dimensional spherocylinder in the Lorentz gas discussed in chapters 3 and 4. These figures expand on the rotational diffusion coefficient and behavior of the tracer as the periodic box size and simulation step size vary. The invariance of the translational diffusion coefficient with respect to box size and time step imply that there is no residual finite size effects in the statistics. The fact that the rotational diffusion is not invariant at constant n^* is an interesting consequence that could be more fully explored in future work. Figures A.8 - A.13 explore how the three dimensional spherocylinder moves in the Lorentz gas, previously discussed in chapters 3 and 4. Specifically, these figures

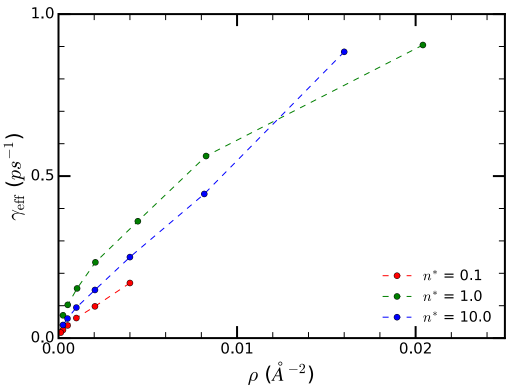

Figure A.1: γ_{eff} vs. number density ρ for a 2D scatterer at various n^*. $\sigma_{\mathrm{T}} = \sigma_{\mathrm{S}} = 0.5$ Angstroms.

look at how varying the box size and time step affect the translational and rotational diffusion and at how the rotational diffusion changes with reduced density. Similarly to the two dimensional case, system parameter invariance implies that finite size effects have been eliminated. In addition, the form of the rotational autocorrelation function in three dimensions implies that Langevin dynamics is not dynamically consistent with the three dimensional Lorentz gas at any friction. Figures A.14 - A.16 detail on how the SHC system previously detailed in chapter 6 equilibrates with respect to system size and equilibration length. The invariance to system parameters provides evidence that the system was large enough and equilibrated long enough to remove any finite size effects. We also detail how the effective RP temperature was fit to a Maxwell-Boltzmann distribution in order to extract the effective temperature.

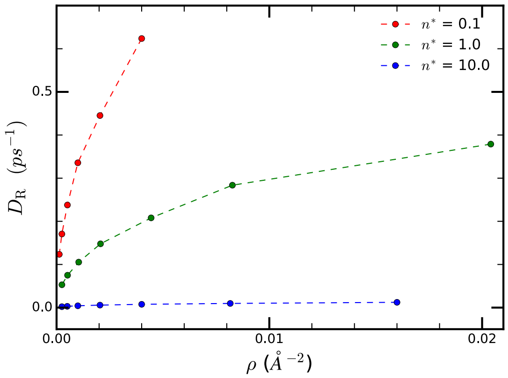

Figure A.2: D_R vs. number density ρ for a 2D scatterer at various n^*. $\sigma_\mathrm{T} = \sigma_\mathrm{S} = 0.5$ Angstroms. D_R is extracted from the RAC via $F_\mathrm{RAC}(\Delta t) = \cos(\omega \Delta t) e^{-2D_\mathrm{R}\Delta t}$.

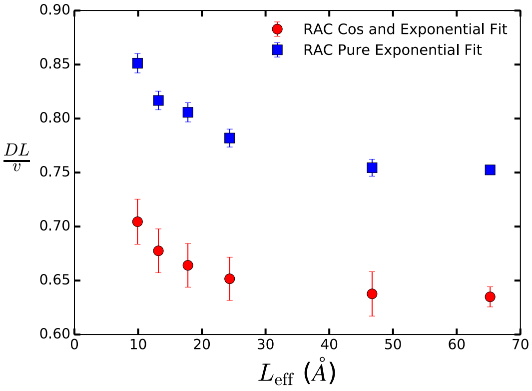

Figure A.3: D_R vs. number density ρ for a 2D scatterer with various L_eff at constant $n^*_\mathrm{ex} = 1$. $\sigma_\mathrm{T} = \sigma_\mathrm{S} = 0.5$ D_R is extracted from the RAC via $F_\mathrm{RAC}(\Delta t) = \cos(\omega \Delta t) e^{-2D_\mathrm{R}\Delta t}$ called the cos and exponential fit and $F_\mathrm{RAC}(\Delta t) = e^{-2D_\mathrm{R}\Delta t}$, which is called the pure exponential fit. D_R is not invariant at constant n^* at low lengths, most likely due to the tracer beginning to approximate a sphere, as spheres have fundimentally different rotational properties compared to spherocylinders.

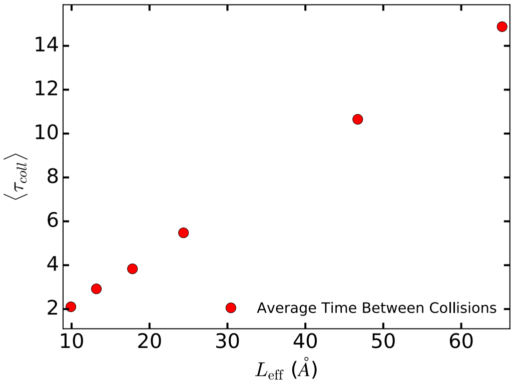

Figure A.4: L_{eff} vs. average collision time $\langle t_{\text{coll}} \rangle$ at constant $n^*_{\text{ex}} = 1$. $\sigma_{\text{T}} = \sigma_{\text{S}} = 0.5$ Angstroms. Note that at constant n^*_{ex}, L_{eff} is inversly proportional to the number density of scatterers, so increasing $\langle t_{\text{coll}} \rangle$ with increasing L_{eff} is not unexpected.

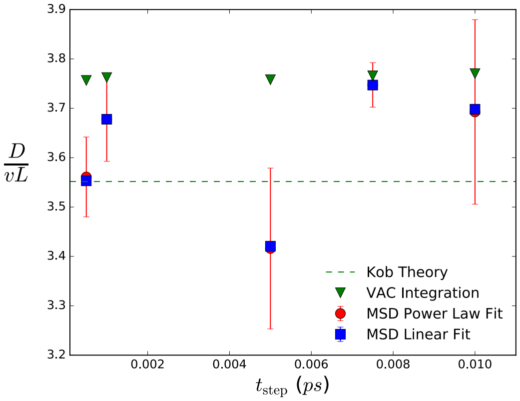

Figure A.5: $\frac{D_{\text{com}}}{vL}$ vs. t_{step}. Although the MSD data is noisy, it is clear that changing the time step size does not effect D.

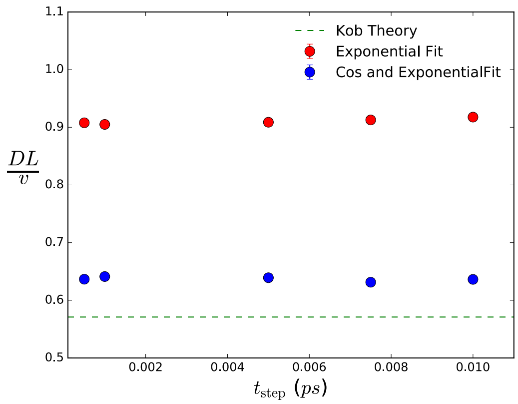

Figure A.6: $\frac{D_{\mathrm{R}}L}{v}$ vs. t_{step}. The reduced rotational diffusion coefficient is clearly not a function of the time step.

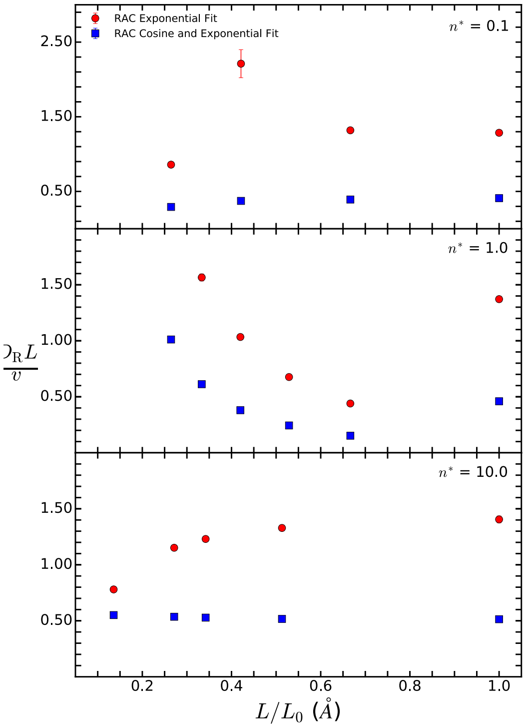

Figure A.7: $\frac{D_{\mathrm{R}}L}{v}$ vs. $\frac{L}{L_0}$ in 3D where L_0 = 7.0, 29.2, 63.0 Å from top to bottom, respectively.

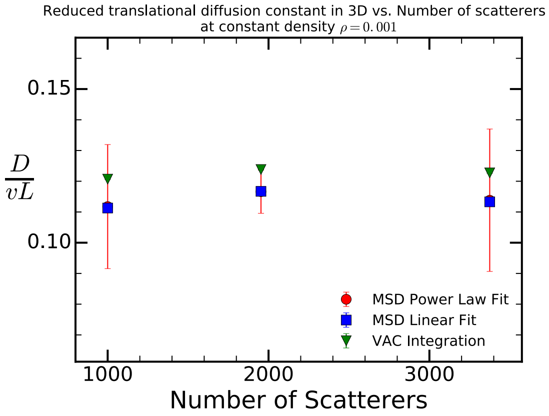

Figure A.8: $\frac{D_{\mathrm{com}}}{vL}$ vs. N at constant density $\rho = 0.001$ in 3D. The flatness implies the box is large enough to ignore finite size effects.

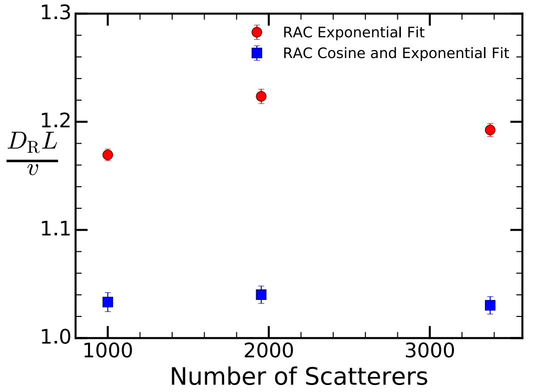

Figure A.9: $\frac{D_{\mathrm{R}}L}{v}$ vs. N at constant density $\rho = 0.001$ in 3D. The flatness implies the box is large enough to ignore finite size effects.

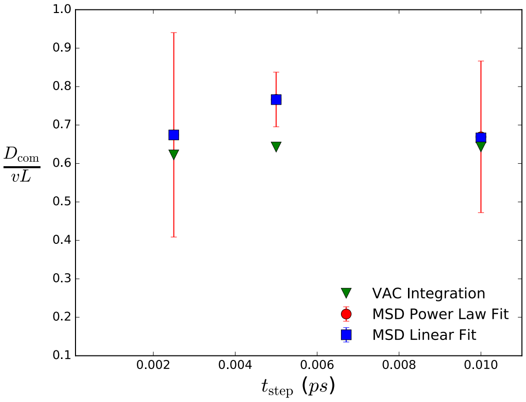

Figure A.10: $\frac{D_{\text{com}}}{vL}$ vs. t_{step}. The flatness implies the stepsize does not cause any issues with the transport.

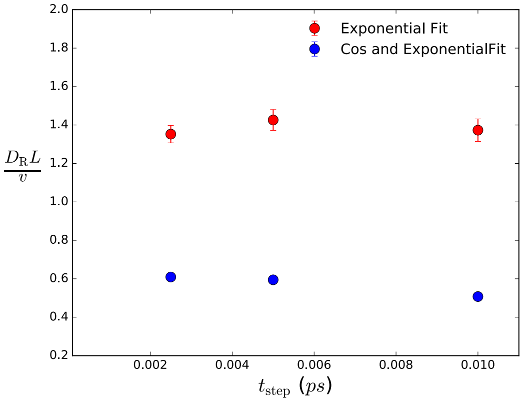

Figure A.11: $\frac{D_{\text{R}}L}{v}$ vs. t_{step}. The flatness implies the stepsize does not cause any issues with the transport.

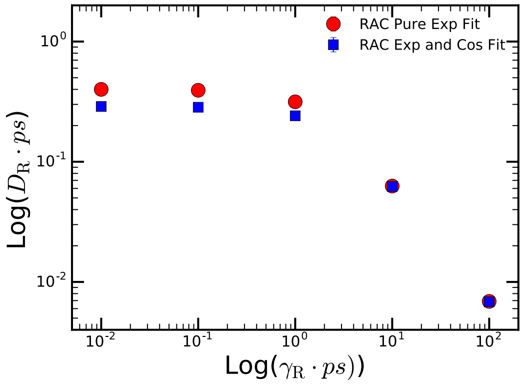

Figure A.12: $\log D_\mathrm{R}$ vs. $\log \gamma_\omega$. For a 2D rod in a pure Langevin solvent with no spheres. At high friction the Debye approximation holds and D_R decreases linearly with friction. At low friction, the system assumes a static equilibrium distribution regardless of friction.

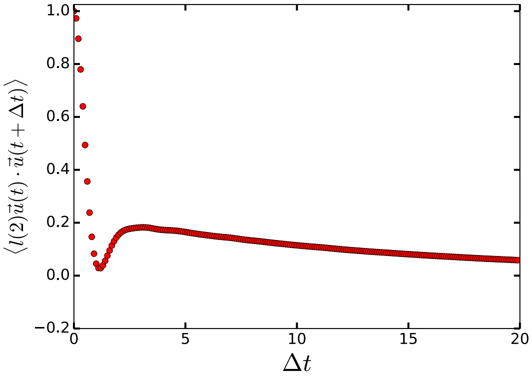

Figure A.13: The Rotational Autocorrelation function with 2^{nd} order Legendre polynomial for a 3D thick tracer in hard spheres with $\gamma n^* = 0.1$. Note the large and long tail that any Langevin system is incapable of generating at any friction. This implies that low density rotational motion in the hard sphere solvent is fundamentally different from rotational motion in a Langevin solvent. It is not possible to map this motion to an effective Langevin friction.

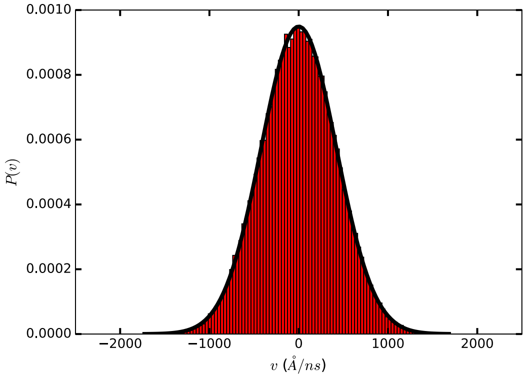

Figure A.14: Characteristic reactive particle velocity distribution post equilibration. $\delta = 0$ 300 scatterers, equilibrated for $10,000$ collisions. The red histogram is the post equilibration velocity of the RP over $100,000$ equilibration trajectories split into 100 bins. The black line is the fit to a Maxwell-Boltzmann velocity distribution with effective temperature of $298K$. Error from $300K$ due to inexact fit and finite bin size. Used for generating post equilibration velocities below.

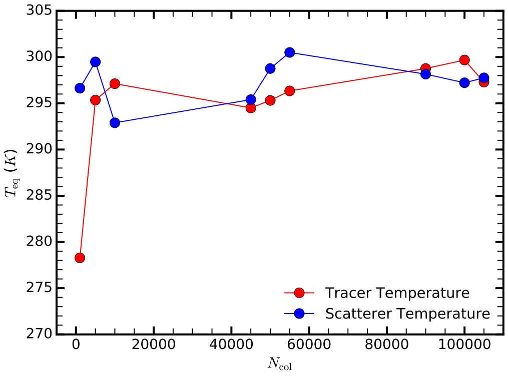

Figure A.15: The average post equilibration temperature for the tracer or scatterers in the SHC system equilibrated in a harmonic well vs. the number of collisions the system is equilibrated for. When the temperature reaches 300 K the system is properly equilibrating. Number of scatterers is 300, $\delta = 0$.

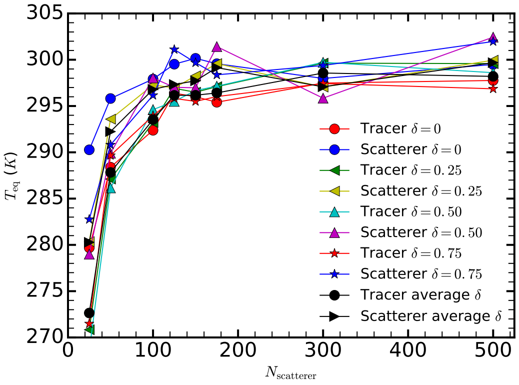

Figure A.16: The average post equilibration temperature of tracers or scatterers in the SHC system equilibrated in a harmonic well vs. the number of scatterers in the system. The movement towards system temperature of 300 implies the vanishing of finite size effects. Equilibrated for $10,000$ collisions.

Curriculum Vitae

Benjamin D. Mahala
Department of Chemistry
Johns Hopkins University
3400 N Charles St
Baltimore, MD 21218

Biographical Sketch:
Place of Birth – Albany, NY
2006 University Academy, Kansas City, MO

Education:

2016-2019	Ph.D. Candidate, Chemistry, Johns Hopkins University
2011-2016	Graduate Research Assistant, Chemistry, Georgia Institute of Technology
2010	B.S. Chemistry, University of Missouri Science and Technology

Publications:
Mahala, B.D.; Hernandez, R. "Order parameters in the diffusion of rods through two- and three-dimensional fixed scatterers"
Phys. Rev. E **98**, 042607 **2018**
Moon J.; Liang, Y.; Stevens T.E.; Monson T.C.; Huber D.L.; **Mahala, B.D.**; Winiarz J.G. "Off-Resonance Photosensitization of a Photorefractive Polymer Composite Using PbS Nanocrystals"
J. Phys. Chem. C **119**, 24, 13827-13835, **2015**

Manuscripts in Preparation:
Mahala, B.D.; Solvent softness effects on unimolecular chemical reaction rate constants" *In preparation*
Mahala, B.D.; Hernandez, R. "Molecular dynamics of a mixed solvent system:

diffusion anomalies and coarse graining" *In preparation*

Presentations:

Summer 2017	American Conference on Theoretical Chemistry, Boston, MA Multiscale and Structured Interactions Affect Diffusion Dynamics. *Poster*
Spring 2016	National Meeting of the American Chemical Society, Division of Physical Chemistry, San Diego, CA Understanding the effects of dimensionality: Spherocylinder diffusion in two and three dimensions. *Poster*

Accomplishments:

Constructed a computational chemistry lab protocol for undergraduate level physical chemistry course (2015)

Took part in an research experience for undergraduates in the National Nanotechnology Infrastructure Network at Georgia Tech (2010-2011)

Was an undergraduate researcher in the Winiarz lab at University of Missouri Science and Technology (2008-2010)